Antenna-Filter-Antenna-Based Structures in Transmit-Arrays and Frequency Selective Surfaces

by

Parinaz Naseri

A thesis submitted in partial fulfillment of the requirements for the degree of

Master of Science
Electromagnetics and Microwaves

Department of Electrical and Computer Engineering
University of Alberta

Abstract

Transmit-array (TA) antennas have shown to be a low-cost, low-profile, and viable solution for point-to-point communication such as in satellite application. The existing work on TA and its unit-cell suffers from various drawbacks including fabrication difficulties and unnecessary losses. The focus of this work is on circularly-polarized (CP) TAs and its goal is to propose a unit-cell with better performance and increased number of supported frequency bands. The proposed unit-cells are antenna-filter-antenna (AFA) elements composing of a receive antenna, a non-radiating resonant structure, and a transmit-antenna operating between the input and output radiating ports. The AFA elements can be configured in non-uniform arrays to implement TA antennas or alternatively configured in uniform arrays to implement Frequency Selective Surfaces (FSS). The AFA can be considered as a spatial filter that can adequately change the amplitude and phase of the incident wave passing through it, whereby both arrays, e.g. FSS and TA, can shape the polarization and/or directivity of the antenna illuminating them. The introduction chapter discusses the existing solutions as TA unit-cells, employed methods, and their shortcomings.

The Chapter two talks about single-band CP TA antenna. We propose a novel unit-cell, besides those currently presented in the literature, to achieve high-gain CP steerable radiation pattern. The required phase shift of a TA is achieved by rotation of its unit-cells. To do so, the incident wave to the TA has to be CP and its sense has to change after passing through the TA. Therefore, the unit-cell is structured in two different TA configurations with different phase distribution across these TAs. The first TA is to diverge the feed's radiation to broadside and the latter one is to concentrate and redirect the source's radiation to -15˚-off broadside. Therefore, the TAs were

put in front of a conventional 2×2 array of sequentially rotated CP patches with gain of 12 dB at f=20.5 GHz. The maximum gain of the first TA is 22dB at broadside and the maximum gain of the second TA is 21.5dB at -15˚-off broadside.

In Chapter 3 we introduce a novel dual-band CP TA unit-cell which manipulates the two orthogonal linear components of a CP wave in a way that they exit with equal magnitude and 180˚ phase difference. Therefore, the polarization of the illuminating wave will change and its phase can be controlled by rotation of the unit-cell. To the best of our knowledge, this unit-cell is the first TA element operating at two different frequency bands with insertion loss better than 1 dB at both and providing continuous 360˚ phase shift in the transmitted wave. This element can be also employed in a uniform array of FSS. Therefore, the FSS will work as a polarization converter at two frequency bands. This application can be useful in GPS navigation system in which having the same polarization on the two sides of a bidirectional CP antenna is important.

Preface

This thesis is an original work by Parinaz Naseri under supervision of Dr. Pedram Mousavi and Dr. Marek Reformat. The research completed in Chapter 2 was designed, simulated, analyzed, and measured by myself. The feed antenna used in Chapter 2 is presented in literature and it was just designed by me for our desired frequency. Also, the slot antenna used in the second section of this chapter was originally proposed by Dr. Pedram Mousavi. The slot antenna was only designed for the specific operational frequency of this thesis by me. Chapter 3 of this thesis was planned by Dr. Pedram Mousavi and designed, analyzed, simulated, and measured by me.

Table of Contents

List of Tables

List of Figures

List of Symbols

Symbol	Definition	First Use
$\Delta\phi$	Phase span	12
Δf_t	Transmission window	12
N	Number of metallic layers	12
Δf	Operational bandwidth	12
$\Delta\phi_d$	Desired phase difference	12
$E_{inc}^{i},\ \ i = 1,2$	Incident electric field from side "i"	21
E_{refl}	Reflected electric field	21
E_{trans}	Transmitted electric field	21
$\hat{a}_x$	Unit vector in x-axis direction	21
$\hat{a}_y$	Unit vector in y-axis direction	21
A_{RH}	Magnitude of right-handed circular polarization wave	21
A_{LH}	Magnitude of left-handed circular polarization wave	21
$A_{xi},\ \ i = 1,2$	Magnitude of x-directed field on side "i"	21
$A_{yi},\ \ i = 1,2$	Magnitude of y-directed field on side "i"	21
$s_{ij}^{mn}, i, j = 1,2\ \&\ m, n = x, y$	Linear-polarized scattering parameters from side "j" to side "i"	21
$T_{co.pol.RH}$	Transmission coefficient of co-polarized right-handed wave	22
$T_{co.pol.LH}$	Transmission coefficient of co-polarized left-handed wave	22
$T_{\substack{cross.pol \\ LH-RH}}$	Magnitude of right-handed transmitted wave from left-handed incident wave	22
$T_{\substack{cross.pol \\ RH-LH}}$	Magnitude of left-handed transmitted wave from right-	22

	handed incident wave	
R_{xy}^{φ}	Rotation matrix	23
φ	Rotation angle of unit-cell	23
f_0	Operational frequency	26
λ_0	Free space wavelength	28
k	Wave number	33
r_0	Distance between feed antenna and center of transmit-array	33
r_{mn}	Distance between feed antenna and mn-located unit-cell on transmit-array	33
x_m	Unit-cell location regarding x-axis	33
y_n	Unit-cell location regarding y-axis	33
θ_d	Tilted pencil beam direction	33
$\varphi_{m,n}$	Required phase shift at mn-located unit-cell on transmit-array	33
$\theta_{m,n}$	Angle θ from feed antenna to mn-located unit-cell on the transmit-array	33

List of Abbreviations

Abbreviation	Description	First Use
TA	Transmit-array	2
RA	Reflect-array	2
CP	Circularly-polarized	3
LP	Linear-polarized	4
AFA	Antenna-filter-antenna	6
FSS	Frequency selective surface	7
ERT	Element rotation technique	12
AR	Axial ratio	13
LHCP	Left handed circular polarized	14
RHCP	Right handed circular polarized	14
F	Focal Distance	14
D	Transmit-array side dimension	14
TE	Transverse electric	24
TM	Transverse magnetic	24
ASRP	Array of sequentially rotated patches	30
PEC	Perfect electric conductor	60

Chapter 1

1 Background

In many applications including satellite communication and point-to-point communications, the radiated power is required to be concentrated in a specific direction so that not only is the transmitted power to the receiver maximized but its interference with other systems operating at the same frequency band will be minimized. For this reason, high-gain and directive antennas with beam agility are demanded. Moreover, the mass market applications require low-cost and compact terminals. While a traditional and simple solution like the combination of a horn antenna and a parabolic reflector serves this purpose for terminals with no limitation of cost and volume, it is an unsuitable answer for so many other applications. The demand for less bulky solutions motivated researches to propose phased arrays [1-4].

Phased-arrays, which are the major part of electronic steering antennas, can be quite low-profile and quickly reconfigurable [5]. These arrays are simply composed of individually excited phase shifting elements. Since a control line is required to for each element, the complexity of the feeding network dramatically increases for large arrays [6]. Besides inevitable complex feeding network of phased-arrays, a great amount of loss, space, and cost, especially at satellite communication frequency band, i.e. Ka-band, gets introduced by the control lines [5]. Although some attempts have been made to reduce the cost of this solution [7], the mechanical steering antennas as the cheapest solutions are more attractive.

Mechanically reconfigurable solutions are mostly composed of multi-panel arrays of patches [8], reflector antennas [9-11], lenses [12-14], or planar structures such as reflect-arrays [15] and transmit-arrays [5]-[16]. The beam steering in these solutions happens by the appropriate movement of either the radiating aperture or the feeds. In multi-panel arrays of patches as opposed to phased-arrays, the beam is steered by moving the structure of the arrays itself rather than a costly reconfigurable feeding network. Also, the radiating surface is divided into small panels to decrease the height of the whole system (See Figure 1.1).

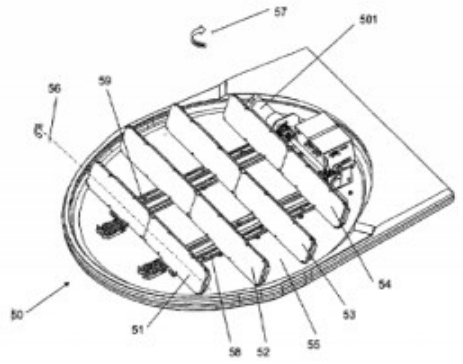

Figure 1.1 Multi-panel array of patches (Taken from [8]).

In lenses, reflectors, reflect-arrays, and transmit-arrays, only a single focal feed is required to excite the radiating structure. Therefore, these solutions overcome the major disadvantage of the phased-arrays by this method. The required high gain in these solutions is achieved by the concentration of the radiation from an average-gain focal source in either reflection mode (in reflectors and reflect-arrays) or transmission mode (lenses and transmit-arrays). The advantage of solutions operating in transmission mode is that they do not suffer from blockage or shadowing the source for specific beam pointing directions [6]. Thus, the angles that can be steered in systems employing lenses and transmit-arrays are not limited by the shadowing effect and include a wider scanning range.

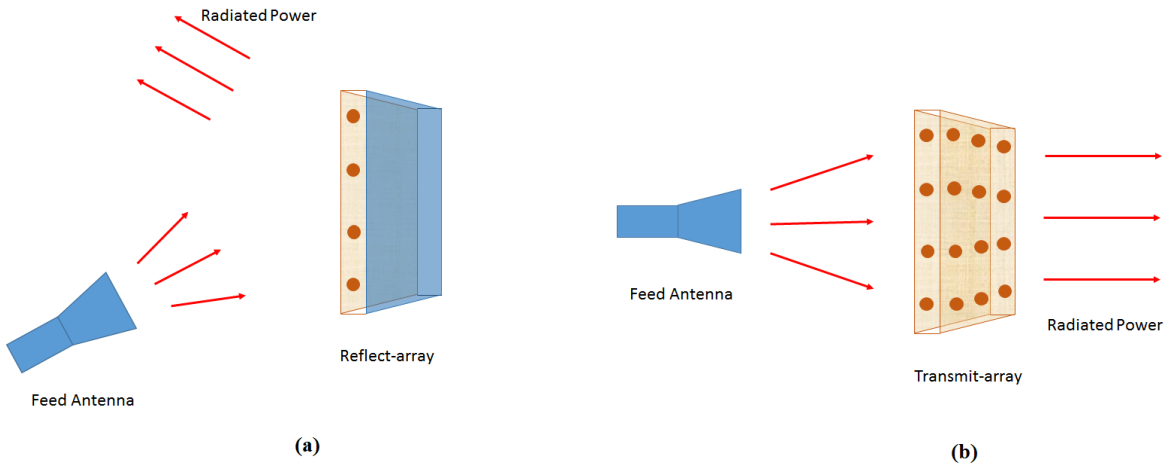

Figure 1.2(a) Planar reflecting solution and (b) planar transmitting solution.

Simple mechanical steering, wide steering angle, and reasonable cost has made dielectric lenses a good candidate for point-to-point communications. Dielectric lenses can be composed of homogenous materials [12] or heterogeneous parts [17]. The beam pointing in lenses can be simply done by moving the lens position in front of a fixed horn antenna [14]. It is reported that the heterogeneous lenses have wider angle coverage than the homogenous ones [6]. Thus, research on designing novel heterogeneous lenses is still an active area especially as new technologies to fabricate non-uniform materials evolve [17]. Moreover, reducing the profile of these lenses has been a motivation for researchers: authors in [18-19] employed non-uniform dielectric lenses to design compact planar structures; furthermore, transformation optics is a recent branch in metamaterials providing a new method for designing compact metamaterial lenses [20].

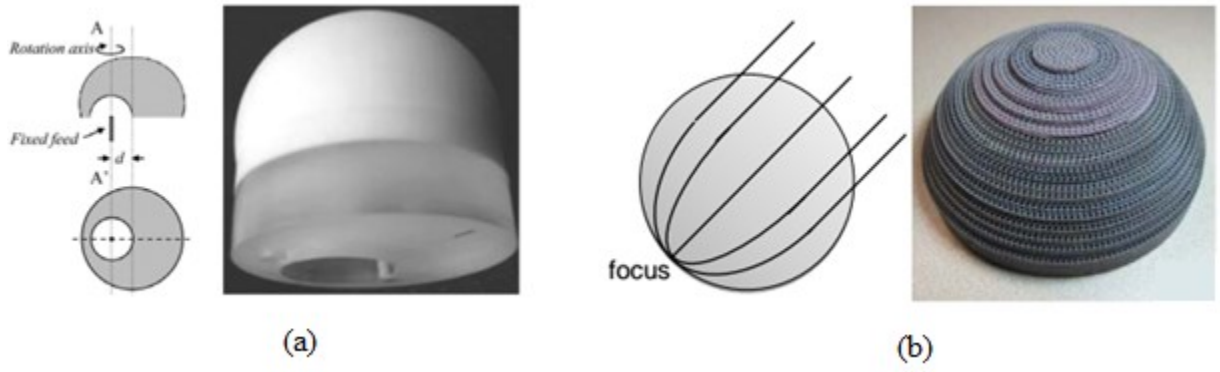

Figure 1.3(a) Homogenous lens and its operation principle (Taken from [12]) and (b) Luneburg lens as a heterogeneous lens and its operation principle (Taken from [17]).

Planar arrays such as reflect-arrays (RAs) and transmit-arrays (TAs) have been proposed to synthesize a large compact effective aperture. In these solutions, an array of non-uniform unit-cells is spatially excited by a single feed antenna. Each unit-cell applies desirable changes to the phase of the incident wave so that a uniform phase distribution across the aperture is created. Due to the mentioned advantages of the transmit-array over reflect-arrays, the focus of this thesis is to propose a low-profile, low-cost, planar transmit-array for satellite communication in Ka-band.

Moreover, since contemporary communication technologies demand for more reliability and assurance, they utilize circularly-polarized (CP) based transmitters and receivers. One of the phenomena causing problem in satellite communication is Faraday rotation effect. Due to Faraday rotation effect, a linearly-polarized electric field experience rotation once it passes through ionosphere. Therefore, this rotation can lead in mismatch between the transmitting wave and the receiving antenna and result in great amount of losses [21]. In addition, a complex adjusting system for antenna alignment requires to be utilized in linear-polarization based point-to-point communication systems like ground based ones. Exploiting CP signals is more reliable

and more efficient since a CP wave only experiences a phase delay and no change in its sense because of Faraday rotation effect [21]. There are abundant designs in literature for TAs to achieve high-gain radiation from a low-directive feed antenna. While some of these existing works achieve linear polarized (LP) high-gain pencil beam radiation from an LP feed [16], there are a few solutions transmitting a CP high-gain power from either an LP or a CP feed antenna [16], [22-23].

The overall design and analysis procedure for a transmit-array-based solution can be divided into three stages [24]:

- Unit-cell design: this step has its own two sub-steps. First, a unit-cell configuration according to the specific physical and electromagnetics constraints, such as substrate thickness, cell size, phase shift range, transmission coefficient, polarization, etc., is proposed. Secondly, a series of the designed unit-cells providing various phase shifts in the transmitted wave are optimized.
- Transmit-array design and model: this stage has also its own two sub-steps. First is to define the theoretical continuous phase correction function according to the gain, scanning losses, and focal length. Secondly, distributing the pre-designed unit-cells with specific phase shift across the transmit-array. Inevitably, the continuous phase correction function has to be discretized according to the size of the unit-cell at this level. The discretization introduces a loss to the performance of the system resulting in decreasing the efficiency of the array. Moreover, as depicted in Figure 1.4, many solutions use 1-bit or 2-bit phase shifters to compensate for the different phase delays required on the surface of a TA. Therefore, whenever any amount of phase shift other than the available phase shift is required, amount of loss and error happens. This is called quantization error or loss. This loss depending on the

size of the unit-cells would reduce the maximum gain of the whole system. A TA antenna using 2-bit phase shifters suffers from 3dB loss in the maximum gain. A cell that can provide continuous phase shift is more desirable since it avoids any quantization loss

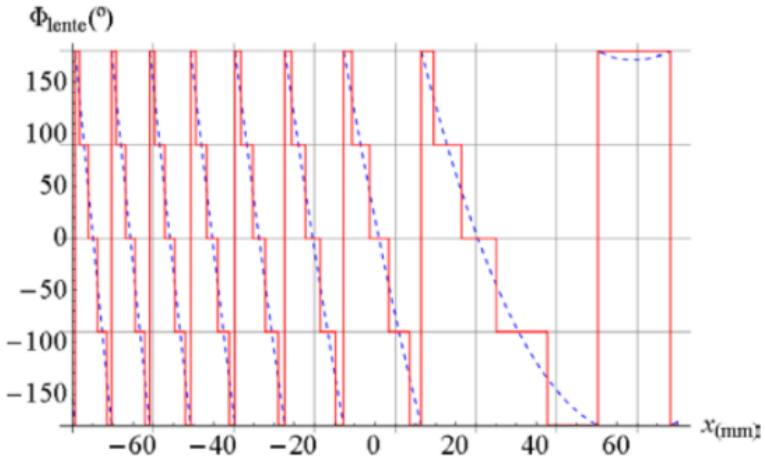

Figure 1.4 Transmit-array phase correction for a continuous phase correction (dashed blue curve) and for a four step phase quantization (red curve) (Taken from [6]).

- Feed and transmit-array model: the designed transmit-array is placed at the focal distance from a suitable feed antenna. The focal length, i.e. the distance between the feed and the TA, determines the spillover loss and taper loss of the system. Thus, it has to be optimized.

The focus of this work is to propose well-designed TA unit-cells based on AFA structure with minimized substrate layers, minimized insertion loss, and continuous phase shift control which operate at one single frequency band and dual frequency bands. Also, a via-less solution is preferred since employing metal via adds to the profile of the whole structure and it also requires accurate and complicated fabrication technologies and methods, especially at higher frequencies. The single-band CP unit-cell is structured in two different TA configurations to achieve high-gain CP power radiating at broadside and 15 degrees off broadside. A thorough analysis on the

design of a dual-band TA unit-cell is also presented in this work which can be used for different applications with different operating frequency bands.

1.1 Analysis of Transmit-Array Cells

There has been an extensive research on transmit-array unit-cells. Each unit-cell exploits various methods and techniques to provide a package of more advantages comparing to existing solutions. To fairly compare different transmit-array elements, J. Y. Lau in [6] suggests that transmit-array unit-cells would be categorized in three groups: “scatteres”, “resonators”, and “antennas with phase shifters/time delayers”.

The beam focusing in the first category of TAs composing of “scatterers” can be obtained by designing the characteristics and distribution of these elements. J. Y. Lau in [5] calls this method “distributed-scatterer” approach. Non-resonant elements can be put in this category. Non-resonant elements have smaller dimensions comparing to the half wavelength of the operating frequency. This category can be employed to design miniaturized structures with less sensitivity to the incident angle of the illuminating wave [25]. The second category of TAs composes of “resonators” [5]. The main key of this category is that the variation in the phase of the transmitted wave is sensitive to the operating frequency or the size of the resonating element. The author of [5] calls this method “coupled-resonator” approach.

The last group of TAs composes of combination of antennas and phase shifters or time delayers. The magnitude of phase (or delay) in each phase shifter (or time-delayer) of an element can be controlled. Therefore, a TA is composed of elements that apply various phase shifts or time delays) to the incident wave. Specifically for elements with time-delayers, one antenna has to receive the incident wave from free-space and couples it to a certain-long transmission line [5].

In [5], this method is called “guided-wave” approach. [26-27] exploit this approach to achieve a wide-band TA unit-cell.

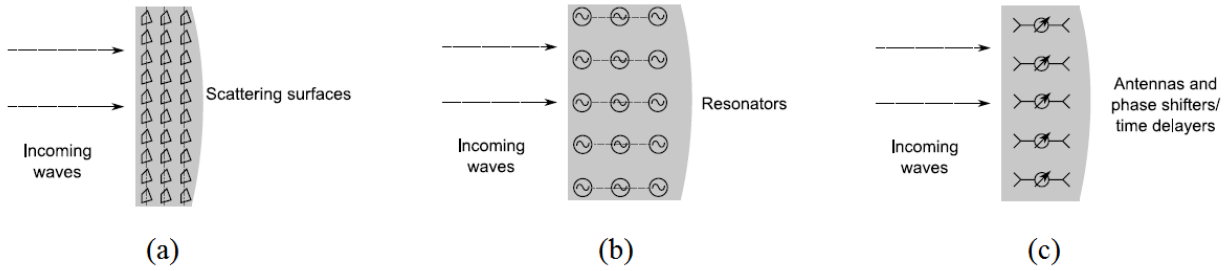

Figure 1.5 TA approaches (Taken from [5]).

On the other hand, we can consider the paths that waves propagate through. Since different media have various corresponding phase velocities, when waves propagate on different path lengths, they experience different time delays or phase shifts [6]. Hence, transmitted waves from a designed lens coming from all the paths incurring the same phase shift or delay to a point converge to that point. Alternatively, Huygen’s principle considers each point in the lens as a radiating element which propagates waves in every direction like an infinite small source induced by the incident wave. The focal point, in this case, is where the radiations from all the elements add constructively [6].

Although not every TA can be put in only one of the above categories, the proposed structures in this thesis are basically based on coupled-resonator approach. [28-34] also use this approach with different forms of resonators. In1960s, passive TA elements composing of two antennas connected by a coaxial transmission line were proposed [28]. Although the arrays were planar, the elements were not low-profile. More recently, elements based on microstrip patch antennas [29-31], and a lens prototype using multiple layers of cross elements [32] were presented. Concurrent to this work, other array lenses are being developed using a wide variety of elements: double square rings [33], patch antennas with perpendicular transmission lines [34], and patch

antennas that transmit a rotated polarization [35]. There are two main approaches to design a transmit-array unit-cell: standard stacked FSS cells and antenna-filter-antenna-based cells. While both groups are considered as FSS [36], there are some differences between them that determines their advantages and disadvantages. In the following subsections, the main differences in the physical and electrical characteristics of these groups are explained.

1.1.1 Resonant FSS Structures

FSS, which is a one- or two-dimensional periodic configuration of unit-cells, demonstrates selectivity over frequency and behave as a spatial filter. Major functionality of FSS structures happens when they operate at their resonance frequencies. Resonant FSS with frequency dependency are either single-layer of patches or slots which can act as band-stop or band-pass filters respectively. [37] models each layer of metallic patches with equivalent induced electric currents while it models single layer of slots in metallic surface by equivalent induced magnetic currents. For our application that the element is meant to be structured in a TA, an array of slots which is transparent in its transmission window and operates as a bandpass filter is required.

Figure 1.6 is illustrating the common patch shapes of FSS elements. However, their complementary shapes in the metallic surface in slot shapes can be used when transmitted signal is required rather than reflected signal [37]. To reduce the level of grate-lobes, the unit-cell size must be smaller than half of free-space wavelength. Hence, according to Figure 1.6, this criteria can eliminate some shapes that require more than this space to operate at their resonances.

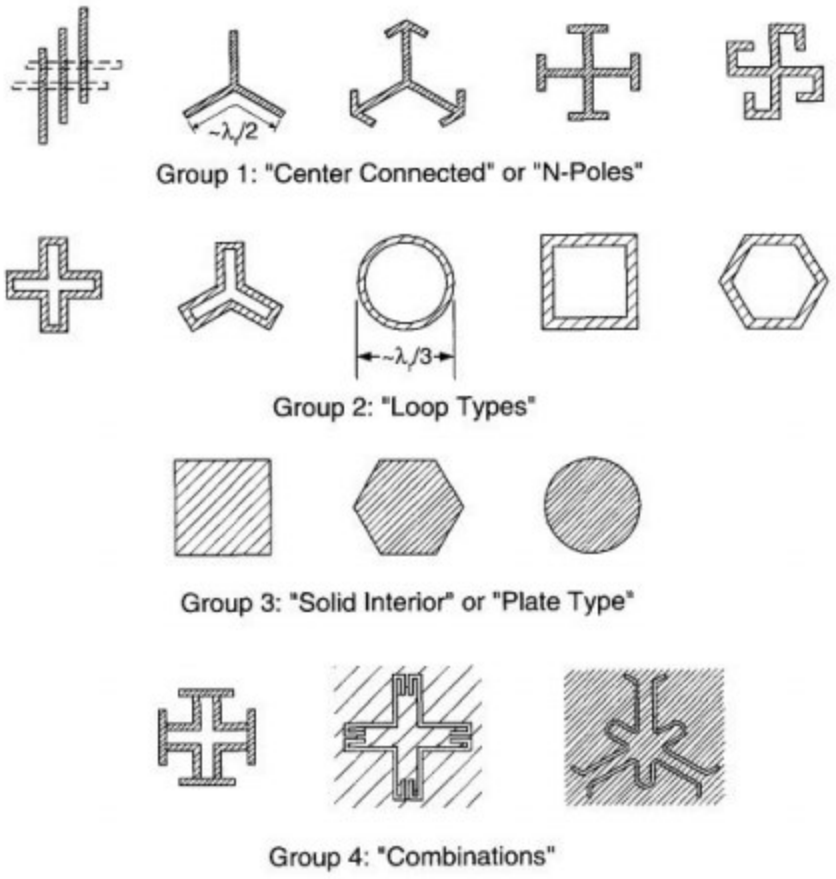

Figure 1.6 FSS structures (Taken from [37]).

Moreover, a CP TA unit-cell can be considered as a time-delay unit between the two linear polarizations. As described in [38-40], miniaturized-element-based frequency selective surfaces have been used for the same purpose. To function in such way, they must provide linear phase responses versus frequency in their transmission window. Therefore, if the proposed unit is designed to exhibit linear phase responses for both x- and y-directed polarizations, it can be structured in a TA surface. Conventionally, researchers have stacked similar FSS layers with thick $(0.2\lambda_0 - 0.3)$ dielectric slabs [36] to implement a TA unit-cell as a spatial filter with acceptable transmission magnitude and bandwidth. These dielectric separators can be considered as simple impedance inverters. Based on the approach that they wish to obtain the phase agility

(explained in the next section) in the TA, the standard FSS structures can become very thick and bulky [36]. For instance, the following brief analysis shows that for additional 45˚ phase difference in the transmission band, one extra FSS layer has to be used. The total phase span ($\Delta\phi$) over the transmission window (Δf_t) can be expressed in terms of number of metallic layers (N) by equation (1.15). Moreover, the operational bandwidth of the cell, Δf, can be written in regard with $\Delta\phi$, Δf_t, and the desired phase difference ($\Delta\phi_d$) [41].

$$\Delta\phi \simeq \frac{N+1}{4}\pi \qquad (1.15)$$

$$\Delta f < \Delta f_t\left(1 - \frac{\Delta\phi_d}{\Delta\phi}\right) \qquad (1.16).$$

In the case that phase rotation technique is used to obtain phase shift in the TA, $\phi_d = 180^\circ$. Both above equations prove that it is unfeasible to achieve this phase difference and zero insertion loss with less than three FSS layers. To improve the performance of the cell such as bandwidth, even more layers are required.

However, the physical bulkiness is not the only drawback of standard FSS approach. Exploiting stacked resonators via impedance inverters can limit the available class of filter responses [36]. For instance, to the best of our knowledge, there are few publications on polarizers with two separate operational frequency bands using one FSS structure. That is why the third chapter of this thesis is a novel contribution. Moreover, due to the near-field coupling between the FSS resonator layers, a filter synthesis of only resonators and impedance inverters can be the first pass in the design procedure. The design procedure has to be followed by detailed and complicated optimization methods to retune the FSS layers and dielectric slabs [36].

1.1.2 Antenna-Filter-Antennas

To avoid drawbacks of conventional stacked FSS structures, spatial filters can be implemented by antenna-filter-antenna-based structures. As the name suggests, an antenna-filter-antenna (AFA) is composed of a receiving antenna, a non-radiating resonant layer, and a transmitting antenna. Each AFA can be considered as a spatial filter manipulating the waves passing through it. AFA elements can help to synthesize a wider range of filtering shapes comparing to the conventional approach. Moreover, the order of the resultant filter can be simply increased by adding slot resonators to the middle layer [36]. The behavior of an AFA can alter according to the direction of the incident electric field. AFAs are generally three-layer metallic structures; two resonant planar antennas at the top and bottom layers, and one or more planar transmission lines or slot resonators in the middle layer [42-44]. The functionality of the middle layer is to couple the top and bottom layers as much as it is to control the characteristics of the final designed filter. Therefore, usage of AFA elements in TAs results in band-pass filters with desirable characteristics for radar, satellite [45], and power combining applications [46].

The major advantage of an AFA element is that key performance factors can be added to the element while maintaining the structure low-profile. For instance, the order of the resulting filter is controllable by the number of the non-radiating resonators in the middle layer [41]. Moreover, the resonance frequency of each AFA element can be changed by adding a varactor to each cell. This approach not only provides phase agility but it also makes the cell reconfigurable [44]. While, the high-order filters are conventionally achieved by stacking resonant frequency selective surface (FSS) structures using thick substrate layers. Not only does this method end in

bulky and heavy structures, which are undesirable for many applications, but the complexity of this method also increases drastically by increased number of layers.

However, as mentioned, all layers of an AFA consist of resonating elements with filtering capabilities regarding frequency or direction of the electric field. Therefore, it is very useful to exploit the existing knowledge in FSS structures to find the suitable element configuration for the application of this thesis. A brief review on common FSS structures is presented in section 1.3.

A suitable AFA element for the structure of the TA must have minimum insertion loss, minimum reflection, and maximum stability regarding the angle of incidence. Moreover, the size of the element or unit-cell has to be smaller than half of free-space wavelength to avoid grating lobes in the transmitted radiation pattern. Last but not the least, it has to provide the ability of phase control on the transmitted wave.

There are different approaches to change the phase of the transmitted wave by altering the a few characteristics of the unit-cell. For instance, [35] is changing the element resonance frequency to alter the transmission phase. In [22], authors use rotation of the unit-cell to achieve phase shift in the transmission coefficient. Since this method provides continuous phase shift in the transmission wave along with minimum required optimization for each cell, it is the focus of this work. It is worth mentioning that this method can only be used when the incident wave is circularly polarized. A thorough explanation on how this method provides phase shift in the transmitted CP signal is presented in next chapter.

1.2 Element Phase Agility

Since waves from a feed source propagate through different path lengths to reach each cell, each cell must have the ability to manipulate the wave passing it. Since the most variation in phase response of a unit-cell happens at its resonance, the interest has been drawn toward passive resonance structures to implement TAs. As explained before, elements with almost linear phase response versus frequency in their transmission windows are desirable.

1.2.1 Resonance Frequency Alteration

Wide range of phase shifts can be acquired by altering the resonance frequency of the cell. Therefore, many different approaches have been proposed to alter the resonance frequency of a unit-cell ranging from a simple dimension alteration [31] to usage of varactor in the cell structure [39]. This method is depicted in Figure 1.7. Moreover, discrete phase distribution across the array surface is usually applied due to great number of optimizations for all cells of the TA. As a result, quantization loss is introduced to the system.

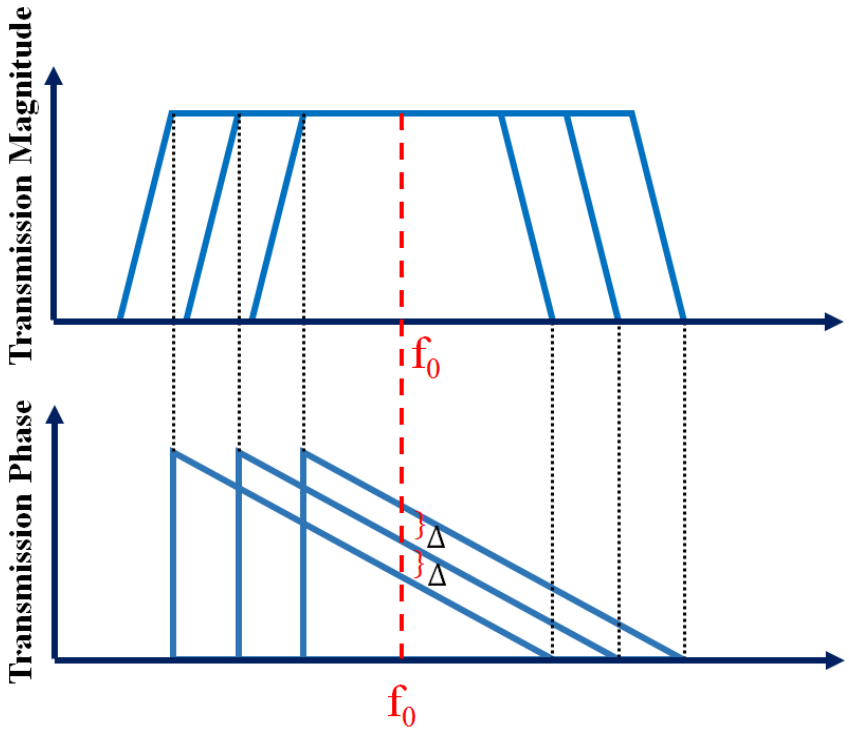

Figure 1.7 Demonstration of achieving phase shift by changing the resonance frequency of unit-cell (Adapted from [47]).

1.2.2 Element Rotation Technique

Element rotation technique (ERT) has been used before to provide phase shift in CP transmitted wave [22-23]. In next chapter, we write the detailed CP coefficients equations in terms of LP coefficients and we show how rotating the unit-cell can help to control the transmission phase. It has to be noted that this method can only be used with CP signals and the sense of the polarization also has to change after passing through the cell. Consequently, a phase shift which is twice the amount of cell rotation angle is obtainable in cross-polarized transmission coefficient.

In [5] with a two layer FSS structure, the required 180˚ phase difference is achieved along with a major insertion loss, e.g. 3dB. [22] employs the same method by designing a 5-layer aperture-

coupled stacked-patch unit-cell. The patches are rectangular with different dimensions along x- and y-axis to become asymmetric and different for two orthogonal linear polarizations. In order to avoid the problem [23] has, authors of [22] take advantage of stacked FSS structures to achieve the design requirements with almost 0dB insertion loss. For all these reasons, we employ an AFA-based element.

1.3 Organization of Thesis

This dissertation consists of four chapters including the introduction chapter. The second chapter proposes a single-band CP TA unit-cell operating at K-band. The required phase shift is achieved by rotating the unit-cell according to its position on the TA surface. As next step, unit-cell is structured in a symmetric TA. The TA is then installed in front of a CP feed source. This chapter discusses the performance of an individual cell in a periodic boundary condition, the TA configuration, and the performance of the feed source and TA combination. Circular-polarized pencil beam radiation toward broadside with 23dB gain and axial ratio (AR) better than 1dB is achieved at 20.5 GHz. To steer the beam, two other TA configurations are implemented to direct the radiation to 15 degree and 30 degree off broadside. The same unit-cell is scaled and structured in FSS. The FSS is combined with a bidirectional CP slot antenna to function as a polarization convertor and achieve same polarization at both sides at 1.7 GHz. Chapter three discusses the design analysis of a dual-band circular-polarized TA unit-cell. This chapter proposes a novel dual-band element based on this analysis which operates at 10.8GHz and 16.7GHz with less than 1dB insertion loss at both bands. The last chapter talks about the significance of this work, possible improvements, and future works.

1.4 Contribution of this thesis

This thesis employs a known category of transmit-array unit-cell structures, antenna-filter-antennas, to introduce a novel simple three-layer TA element. This element provides various advantages comparing to the solutions presented in the literature. Firstly, this cell applies transmission loss of close to 0 dB to normal incident wave although it is only composed of three metallic layers. Secondly, the required phase shift in the transmitted wave is simply provided by rotation of the cell which is achievable up to 360°. While the cell applies the required phase correction to the CP wave, it changes its sense of polarization.

We structured this cell into a TA configuration to concentrate the radiation of a focal source to different angles. Furthermore, we exploited the ability of the cell that changes the sense of the CP wave to design a same-sense CP bidirectional antenna. Finally, by small modifications in the structure of the cell, we introduced a novel dual-band TA unit-cell for CP applications. In conclusion, this thesis takes a further step in exploring the advantages of antenna-filter-antenna-based elements and employs the proposed structures for different applications to prove this claim.

Chapter 2

2 Single–Band Circularly–Polarized Unit–Cell Structured in Transmit–Array and FSS

As discussed in Chapter 1, for many point-to-point communications especially satellite application, the power is required to be CP, high-gain and directed to a specific direction. A viable solution to meet these demands is installing a TA, also known as discrete lens, in front of a low-gain CP feed antenna.

In this chapter, a detailed study of ERT to achieve phase agility is presented. Based on this method, a novel CP unit-cell with CST Studio software using periodic boundary conditions is designed. The cell is then configured in two different TAs to transmit power to broadside, 15 degree off broadside directions. A conventional 2×2 array of sequentially rotated CP truncated patches is combined with each of the designed TAs to transmit CP directive beam (See Figure 2.1).

The TA is designed to function like a flat zoned-lens. It focuses the radiated CP signal from the feed antenna to a certain direction while changing the sense of the CP wave. For instance, the illuminating right-handed-circular-polarized (RHCP) radiation power with 13dB gain is changed to a left-handed-circular-polarized (LHCP) wave with 23dB gain after propagating through the TA. The discrete lenses are 14×14 arrays of the proposed element. Then, the TAs are placed in focal distance (F) from the feed antenna. The focal distance (F) to TA dimension (D) ratio is set to 0.8.

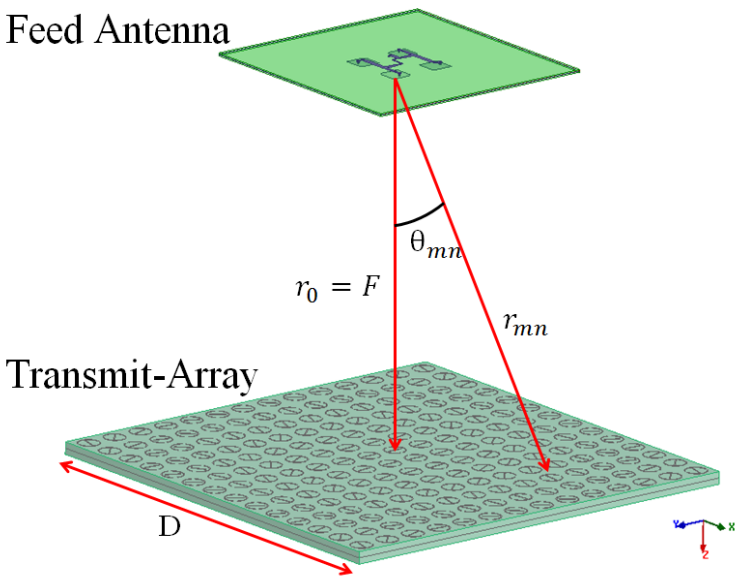

Figure 2.1 TA system structure composing of feed antenna and TA.

Furthermore, the same cell is structured in a 3-by-3-element FSS configuration to act as a polarization convertor. The FSS is placed in close proximity of a simple CP bidirectional slot antenna (See Figure 2.2) to achieve bidirectional CP antenna with same polarization at both sides. As in many applications such as GPS navigation systems, only one sense of CP signal is desirable and the other is considered as a bad signal [21].

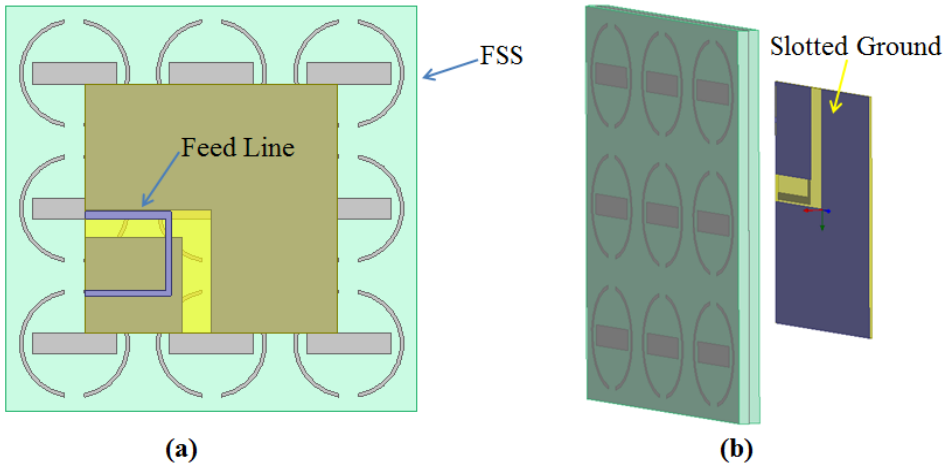

Figure 2.2 Same sense bidirectional antenna composing of slot antenna and polarization converting FSS.

2.1 Element Rotation Technique

To understand how ERT provides phase shift in the CP transmitted signal, we write the rotated CP scattering parameters (S-parameters) in terms of LP S-parameters and cell rotation angle. We also drive these equations to realize the physical requirements of a suitable element for our application. The equations are either derived from basic mathematics or taken from mentioned references ([22] and [48]). Figure 2.3 illustrates a general medium being excited by arbitrarily-directed electric fields from both directions. Considering the medium as a two-port network, the the incident waves, reflected wave, and transmitted wave can be related by scattering parameters of a scattering matrix. The E_{inc}^{1} and E_{inc}^{2} incite the medium from left side and right side, respectively. E_{ref}^{1} is the sum of the reflected wave of E_{inc}^{1} and the transmitted wave of E_{inc}^{2} on the left side. E_{trans}^{1} is the sum of the reflected wave of E_{inc}^{2} and the transmitted wave of E_{inc}^{1} on the right side.

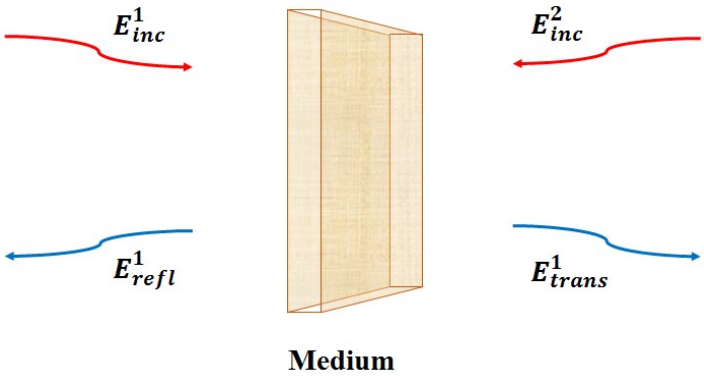

Figure 2.3 General medium illuminated by arbitrarily-directed waves.

$$\begin{bmatrix} E^1_{refl} \\ E^1_{trans} \end{bmatrix} = \begin{bmatrix} S_{11} & S_{12} \\ S_{21} & S_{22} \end{bmatrix} \begin{bmatrix} E^1_{inc} \\ E^2_{inc} \end{bmatrix} \qquad (2.1)\ [48]$$

$$E^1_{inc} = \left[A_{RH1}(\hat{a}_x - j\hat{a}_y) + A_{LH1}(\hat{a}_x + j\hat{a}_y)\right]e^{-jkz} = [A_{x1}\,\hat{a}_x + A_{y1}\,\hat{a}_y]e^{-jkz} \qquad (2.2)$$

$$E^2_{inc} = \left[A_{RH2}(\hat{a}_x + j\hat{a}_y) + A_{LH2}(\hat{a}_x - j\hat{a}_y)\right]e^{+jkz} = [A_{x2}\,\hat{a}_x + A_{y2}\,\hat{a}_y]e^{+jkz} \qquad (2.3)$$

, where $\mathbf{E^1_{inc}}$ and $\mathbf{E^2_{inc}}$ are arbitrarily and they propagate in +z direction. Therefore,

$$\begin{cases} A_{x1} = A_{RH1} + A_{LH1} \\ A_{y1} = j(A_{LH1} - A_{RH1}) \end{cases} \qquad (2.4)$$

$$\begin{cases} A_{x2} = A_{RH2} + A_{LH2} \\ A_{y2} = j(A_{RH2} - A_{LH2}). \end{cases} \qquad (2.5)$$

We can write the transmitted wave as following:

$$E^{Trans}_{x2} = [S^{xx}_{22}\,A_{x2} + S^{xx}_{21}\,A_{x1} + S^{xy}_{21}\,A_{y1} + S^{xy}_{22}\,A_{y2}]e^{-jkz} \qquad (2.6a)$$

$$E^{Trans}_{y2} = [S^{yy}_{22}\,A_{y2} + S^{yy}_{21}\,A_{y1} + S^{yx}_{21}\,A_{x1} + S^{xy}_{22}\,A_{x2}]e^{-jkz}. \qquad (2.6b)$$

Using (2.4) and (2.5) in (2.6a) and (2.6b) result in following equations (2.7a) and (2.7b):

$$E_{x2}^{Trans} = [S_{22}^{xx}\,(A_{RH2} + A_{LH2}) + S_{21}^{xx}\,(A_{RH1} + A_{LH1}) + jS_{21}^{xy}\,(A_{LH1} - A_{RH1}) + jS_{22}^{xy}\,(A_{RH2} - A_{LH2})]e^{-jkz} \quad (2.7a)$$

$$E_{y2}^{Trans} = [jS_{22}^{yy}\,(A_{RH2} - A_{LH2}) + jS_{21}^{yy}\,(A_{LH1} - A_{RH1}) + S_{21}^{yx}\,(A_{RH1} + A_{LH1}) + S_{22}^{xy}\,(A_{RH2} + A_{LH2})]e^{-jkz} = [A_{RH1}(S_{21}^{yx} - jS_{21}^{yy}) + A_{LH1}(S_{21}^{yx} + jS_{21}^{yy}) + A_{RH2}(S_{22}^{xy} + jS_{22}^{yy}) + A_{LH1}(S_{22}^{xy} - jS_{22}^{yy})]e^{-jkz} \quad (2.7b)$$

Adding the two dimensions, we can write the transmitted wave as below:

$$\begin{aligned} E^{Trans} &= (\hat{a}_x - j\hat{a}_y)[T_{co.Pol.RH}\,A_{RH1} + T_{\substack{cross.Pol\\RH-LH}}\,A_{LH1} + \Gamma_{co.Pol.RH}\,A_{RH2} + \Gamma_{cross.Pol}\,A_{LH2}] \\ &+(\hat{a}_x + j\hat{a}_y)[T_{co.Pol.LH}\,A_{LH1} + T_{\substack{cross.Pol\\LH-RH}}\,A_{RH1} + \Gamma_{co.Pol.LH}\,A_{LH2} + \Gamma_{cross.Pol}\,A_{RH2}] \\ &= \hat{a}_x[A_{RH1}\left(T_{Co.Pol.RH} + T_{\substack{Cross.Pol\\LH-RH}}\right) + A_{LH1}\left(T_{\substack{Cross.Pol\\RH-LH}} + T_{Co.Pol.LH}\right) \\ &+A_{RH2}(\Gamma_{Co.Pol.RH} + \Gamma_{Cross.Pol}) + A_{LH2}(\Gamma_{Cross.Pol} + \Gamma_{Co.Pol.LH})] \\ &+j\hat{a}_y[A_{RH1}\left(T_{\substack{Cross.Pol\\LH-RH}} - T_{Co.Pol.RH}\right) + A_{LH1}\left(T_{Co.Pol.LH} - T_{\substack{Cross.Pol\\RH-LH}}\right) \\ &+A_{RH2}(\Gamma_{Cross.Pol} - \Gamma_{Co.Pol.RH}) + A_{LH2}(\Gamma_{Co.Pol.LH} - \Gamma_{Cross.Pol})] \end{aligned} \quad (2.8)$$

Hence,

$$T_{\substack{Cross.Pol\\LH-RH}} = \frac{1}{2}(S_{21}^{xx} - S_{21}^{yy}) - \frac{j}{2}(S_{21}^{xy} + S_{21}^{yx}) \quad (2.9a)$$

$$T_{\substack{\text{Cross.Pol}\\ \text{RH-LH}}} = \frac{1}{2}\left(S_{21}^{xx} - S_{21}^{yy}\right) + \frac{j}{2}\left(S_{21}^{xy} + S_{21}^{yx}\right) \quad (2.9b)$$

$$T_{\text{Co.Pol.RH}} = \frac{1}{2}\left(S_{21}^{xx} + S_{21}^{yy}\right) + \frac{j}{2}\left(-S_{21}^{xy} + S_{21}^{yx}\right) \quad (2.9c)$$

$$T_{\text{Co.Pol.LH}} = \frac{1}{2}\left(S_{21}^{xx} + S_{21}^{yy}\right) + \frac{j}{2}\left(S_{21}^{xy} - S_{21}^{yx}\right) \quad (2.9d)$$

$$\Gamma_{\text{Cross.Pol}} = \frac{1}{2}\left(S_{22}^{xx} + S_{22}^{yy}\right) \quad (2.9e)$$

$$\Gamma_{\text{Co.Pol.RH}} = \frac{1}{2}\left(S_{22}^{xx} - S_{22}^{yy}\right) + jS_{22}^{xy} \quad (2.9f)$$

$$\Gamma_{\text{Co.Pol.LH}} = \frac{1}{2}\left(S_{22}^{xx} - S_{22}^{yy}\right) - jS_{22}^{xy} \quad (2.9g)$$

In a practical case, S_{21}^{xy} and S_{21}^{yx} are close to zero. Moreover, if we rotate an asymmetric cell for φ degree, as depicted in Figure 1.5, a new xy-coordinate system can be defined. The axes of new coordinate system are rotated φ degree from the previous axes. Hence, the rotated LP scattering parameter matrix, notated as S_{LP}^{φ}, can be driven by S_{LP} and R_{XY}^{φ} [22],

$$S_{LP}^{\varphi} = \left[R_{XY}^{\varphi}\right]^{-1} S_{LP} \left[R_{XY}^{\varphi}\right] \quad (2.10)$$

where S_{LP} is the simplified LP scattering parameters matrix and R_{XY}^{φ} is a rotation matrix,

$$S_{LP} = \begin{bmatrix} S_{22}^{xx} & 0 & S_{21}^{xx} & 0 \\ 0 & S_{22}^{yy} & 0 & S_{21}^{yy} \\ S_{21}^{xx} & 0 & S_{22}^{xx} & 0 \\ 0 & S_{21}^{yy} & 0 & S_{22}^{yy} \end{bmatrix} \quad (2.11)$$

and

$$R_{XY}^{\varphi} = \begin{bmatrix} \cos\varphi & -\sin\varphi & 0 & 0 \\ \sin\varphi & \cos\varphi & 0 & 0 \\ 0 & 0 & \cos\varphi & \sin\varphi \\ 0 & 0 & -\sin\varphi & \cos\varphi \end{bmatrix} \qquad (2.12).$$

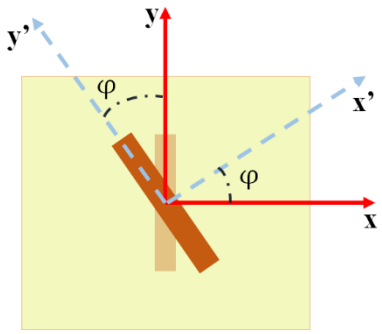

Figure 2.4 Rotated asymmetric unit-cell.

Finally with using equations (1.9)-(1.12), we can drive the rotated CP scattering parameters

$$S_{11}^{lr} = S_{11}^{rl} = S_{22}^{lr} = S_{22}^{rl} = \frac{1}{2}(S_{22}^{xx} + S_{22}^{yy}) \qquad (2.13a)$$

$$S_{12}^{rr} = S_{12}^{ll} = S_{21}^{ll} = S_{21}^{rr} = \frac{1}{2}(S_{21}^{xx} + S_{21}^{yy}) \qquad (2.13b)$$

$$S_{11}^{rr} = S_{22}^{ll} = \frac{1}{2}(S_{22}^{xx} - S_{22}^{yy})e^{+2j\varphi} \qquad (2.13c)$$

$$S_{11}^{ll} = S_{22}^{rr} = \frac{1}{2}(S_{22}^{xx} - S_{22}^{yy})e^{-2j\varphi} \qquad (2.13d)$$

$$S_{12}^{rl} = S_{21}^{lr} = \frac{1}{2}(S_{21}^{xx} - S_{21}^{yy})e^{+2j\varphi} \qquad (2.13e)$$

$$S_{12}^{lr} = S_{21}^{rl} = \frac{1}{2}(S_{21}^{xx} - S_{21}^{yy})e^{-2j\varphi} \qquad (2.13f)$$

We assume that the only incident wave is RHCP signal illuminating the rotated unit-cell. Hence, equations (2.13b) and (2.13e) help us to calculate the portion that transmits as RHCP signal and the rest that transfers as LHCP signal.

Equation (2.13b) proves that cell rotation has no impact on the phase of the transmitted RHCP signal calculated by coefficient S_{21}^{rr}. On the other hand, phase of the LHCP signal calculated by coefficient S_{21}^{lr} is completely controllable by angle of cell rotation, e.g. φ, and it changes twice the amount of cell rotation angle. This analysis proves that we can easily obtain up to 360˚ phase shift in the transmitted signal if we design the element in a way that no CP signal with the same sense as incident wave can propagate through the cell. In other words [22],

$$S_{21}^{rr} = 0 \quad => \quad S_{21}^{xx} = -S_{21}^{yy} \quad \text{and} \quad S_{21}^{lr} = S_{21}^{xx}\, e^{+2j\varphi} \qquad (2.14)$$

It has to be noted that the cell rotation method can only be used for CP signals and the sense of the polarization has to change through transmission. To implement this method, we have to design an asymmetric unit-cell that behaves differently for x- and y-directed electric field embedded in CP signal. To be specific, unit-cell has to transfer the two orthogonal linear parts of a CP incident wave with equal magnitude and 180˚ phase difference at the desired frequency. Thus, researches have employed various asymmetric resonant structures such as split-rings [28-29]. Specifically in [28], the element is based on two-layer slot split-rings and has slightly different resonance frequencies for the two LP signals. By controlling the difference between the two resonant frequencies, 180˚ phase difference in transmission coefficients is achieved. This approach is depicted in Figure 2.5.

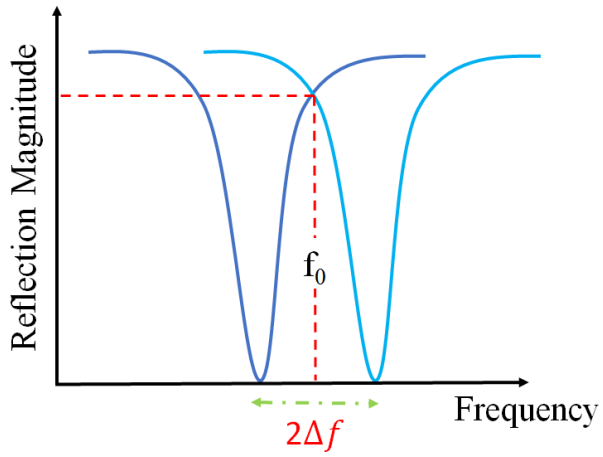

Figure 2.5 Achieving phase difference between two transmitted orthogonal LP signals by introducing slightly difference in resonance frequencies of the cell once it is illuminated by each of them.

It can be seen from Figure 2.5, as we increase the difference between the resonance frequencies to enlarge the phase difference between the transmission coefficients, the meeting point of the reflection coefficients goes higher. This fact in case of structures like [28] and [49-50], which is composed of a two-layer FSS structure, leads to acquiring 180˚ phase difference along with major insertion loss, e.g. 3dB. [22] employs the same method by designing a five-layer aperture-coupled stacked-patch unit-cell. The patches are rectangular with different dimensions along x- and y-axis to become asymmetric and different for two orthogonal linear polarizations. In order to avoid the problem [28] has, authors of [22] take advantage of stacked FSS structures to achieve the design requirements plus almost 0dB insertion loss. To design a low-profile cell with minimum insertion loss, we employ AFA element according to introduction given in chapter 1.

2.2 Single-Band Circular-Polarized Transmit-Array

In this section, we propose a novel single-band unit-cell which behaves differently to x- and y-directed electric field to meet the requirements mentioned in previous section. As a result, ERT can be utilized so that the unit-cell functions as a phase shifter. The unit-cells with different rotation angles are then placed in a TA structure and put in front of a feed antenna to converge and redirect the radiation to a desirable angle.

2.2.1 Single-Band CP Unit-Cell Design

As mentioned earlier, we require to design an asymmetric unit-cell which behaves differently for the two orthogonal linear polarizations. The cell requires transmitting the two LP waves with equal magnitude and 180˚ phase difference. Before introducing the proposed structure, we demonstrate the general steps to implement a cell that is based on antenna-filter-antenna structure, functions as pass-band filter, and behaves differently for the two orthogonal linear polarized incident waves so that it would be compatible to be used with element rotation technique.

Let us consider a simple AFA-based structure that is composed of two rings as receive and transmit antennas coupled through a circular slot (please see Figure 2.6 (a)). The three elements of the cell resonate and provides a zero in the reflection coefficient as it can be seen in Figure 2.7. Since the cell is symmetric regarding x and y axes, its response to TE (x-directed incident wave) and TM (y-directed incident wave) is the same and there is no phase difference in the two transmitted waves. Now, by applying asymmetry to the structure so that it looks like the cell in Figure 2.6(b), the response of the cell to TE and TM waves differ and that introduces phase

difference in transmission coefficients. Figure 2.8 shows the reflection coefficients and transmission phases of the two TE and TM incident waves. It can be seen that at 20.1GHz which is the meeting point of the reflection coefficients, the phase difference between the transmission coefficients is less than 150˚ and the bandwidth of one of the reflection coefficients is very narrow. Although one can argue to change the split length to increase the asymmetry and the consequent phase difference between to the two polarizations, this change leads to a lower CP transmission coefficient.

Therefore, by adding an extra element like a thin grid perpendicular to the axis of the splits, we can introduce additional asymmetry to the structure and achieve the required 180˚ phase difference. This structure is represented in Figure 2.6 (c). Since the grid in parallel to y-axis, TM incident wave excites the grid and the grid's length adds to the average length of the resonator in the receive layer. Consequently, we can see in Figure 2.9 (a) that the first resonance frequency of the third cell is lower than the same resonance frequency of the second cell. Figure 2.9 (b) demonstrates that we can achieve 180˚ phase difference between the two transmissions at the meeting point of the two reflection coefficients.

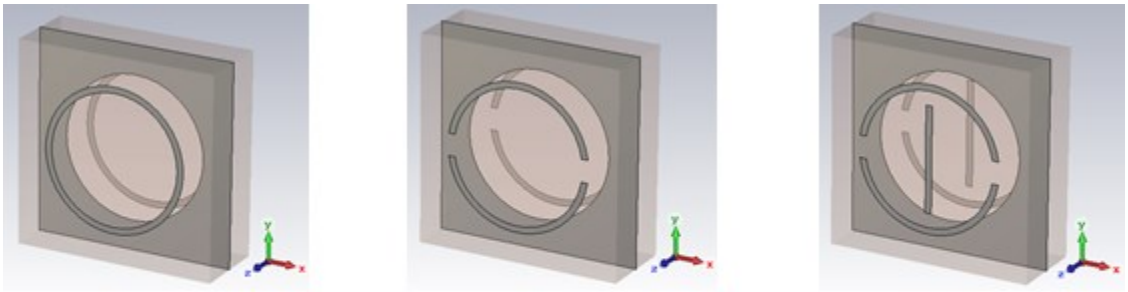

Figure 2.6 Design steps of an AFA-based element as a CP TA element: (a) symmetric element, (b) asymmetric element to achieve phase difference between x- and y-directed transmitted

waves, and (c) asymmetric element to achieve 180˚ phase difference between the two orthogonal linear transmitted waves.

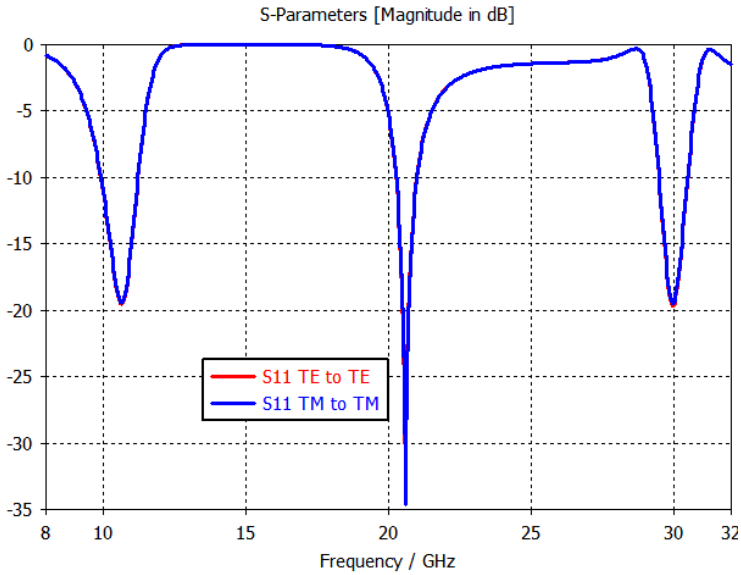

Figure 2.7 Reflection coefficients of the symmetric cell presented in Figure 2.6 (a) to the TE and TM incident waves.

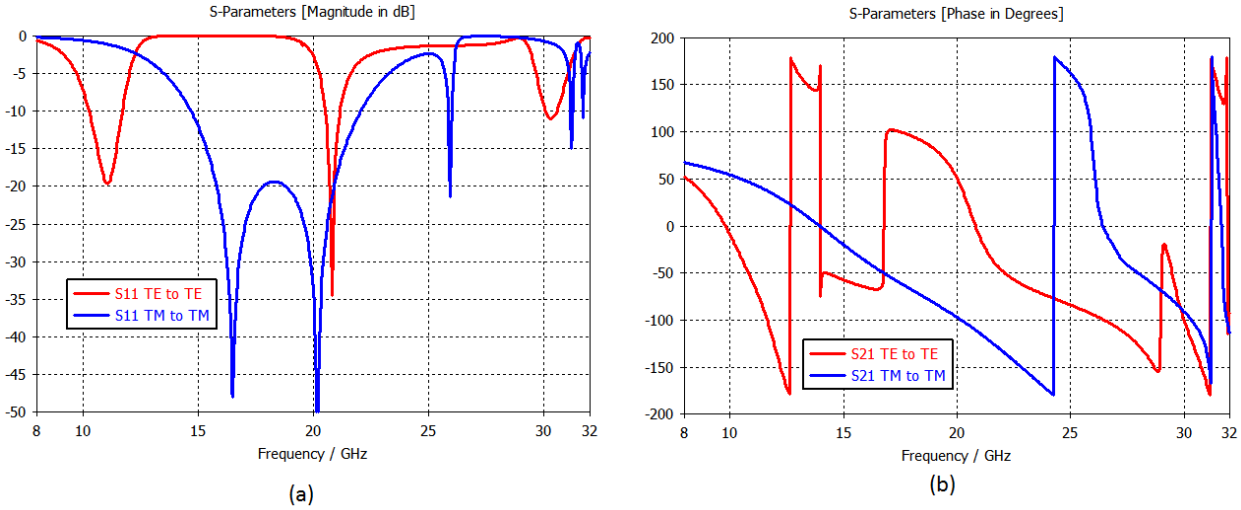

Figure 2.8 (a) Reflection coefficients and (b) transmission phases related to the TE and TM incident waves in cell depicted in Figure 2.6 (b).

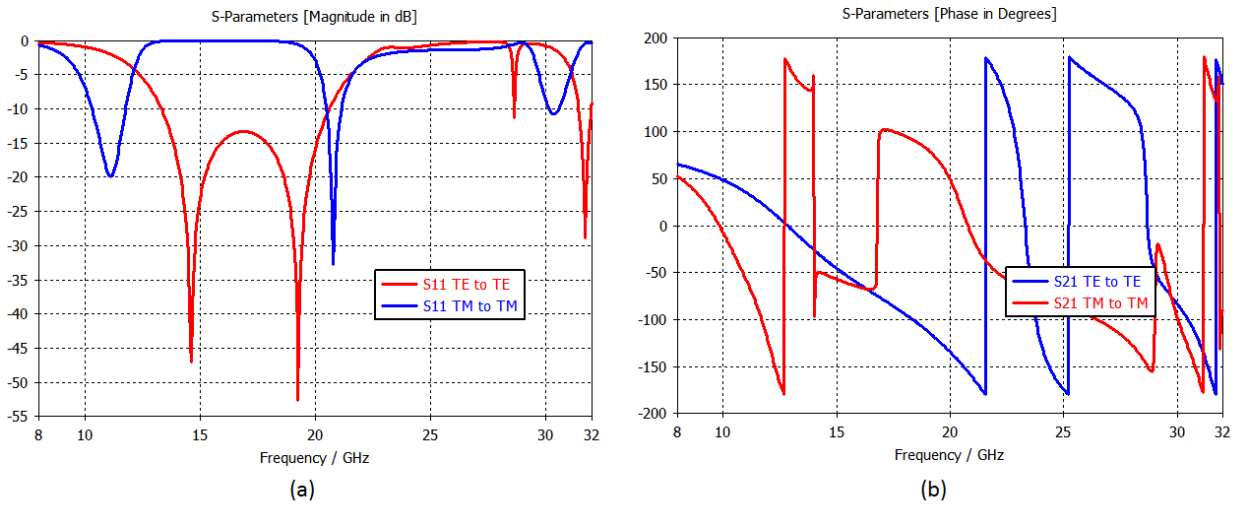

Figure 2.9 (a) Reflection coefficients and (b) transmission phases related to the TE and TM incident waves in cell depicted in Figure 2.6 (c).

The combination of microstrip split rings and grids was employed before to reflect the CP-polarized wave [51-52]. The rotation of each cell was used in [51-52] to correct the phase of the receiving wave and achieve "cophasal beam" at broadside. However, we require a structure that functions in the transmitting mode. Therefore, inspired by the proposed structures in [51-52] and following the aforementioned steps, we designed a CP TA element shown in Figure 2.10 (a)-(c). Figure 2.1010 (d)-(e) depict the surface currents of the structure at 20.7 GHz when it is illuminated by TE and TM incident waves respectively. Figure 2.10 (d)-(e) show the resonating grids, split rings, and circular slot at this frequency.

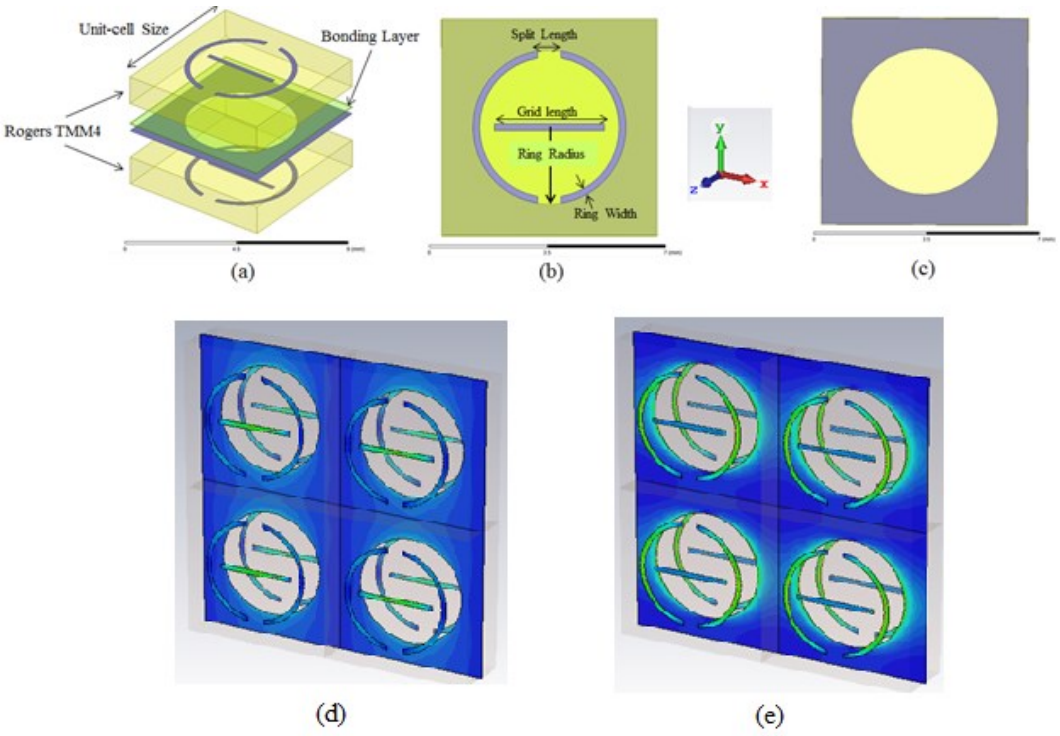

Figure 2.10 AFA structure based on thin grid and split ring antennas and resonating circular slot, (a) 3D structure, (b) top and bottom layers, (c) middle layer, and display of the surface currents on the metal components of the unit-cell in a periodic structure at 20.7 GHz for (d) x-polarized incident wave and (e) y-polarized incident wave.

While the thin grid resonates for the x-polarized incident wave (See Figure 2.10 (d)), the circular slot and the split ring resonates for a y-polarized incident wave (See figure 2.10(e)). The size of each element corresponds to the half wavelength of the wave going through the equivalent dielectric. The equivalent dielectric, here, is defined by the combination of the air and the substrate layers. Therefore, the two linear-polarized waves see the structure differently. This can be translated to that the structure presents two different filters for the two orthogonal incident waves. These two filters have the same magnitude and 180° phase difference at the desired operating frequency. As a result, rotation of the unit-cell, which means the rotation of both first and third layers with the same angle, applies phase shift to the circular-polarized incident wave

and changes its sense.

The dimensions of the structure are optimized with commercial software CST Microwave Studio and are summarized in Table 2.1. It is worth mentioning that the width of unit-cell is chosen to be 6.47mm, %44.6 of free-space wavelength at 20.7 GHz. Substrate layers are Rogers TMM4 with permittivity constant of 4.5 and tangent loss of 0.002. This dielectric choice particularly helps to fit elements in a unit-cell width less than half-wavelength at k-band. Periodic boundaries were applied on the four sides of the unit-cell to simulate an infinite array of elements. Two Floquet ports were applied to the top and bottom faces $\frac{\lambda_0}{4}$, λ_0 is free-space wavelength at 20.7 GHz, distant from the unit-cell surfaces. These two ports illuminate the unit-cell with two orthogonal normal incident waves, transverse electric field (TE_{00}), x-directed wave, and transverse magnetic field (TM_{00}), y-directed wave.

Table 2.1

Single-Band TA Unit-Cell Dimensions

unit-cell width	6.47 mm	ring width	0.2 mm
grid length	3.3 mm	split length	0.7 mm
ring radius	2.3 mm	substrate thickness	1.27 mm

We designed the unit-cell to operate at 20.7GHz suitable for satellite communication. Figure *2.11*1 shows the magnitudes and phases of the transmission coefficients for TE_{00} and TM_{00} incident waves. Figure *2.11*1 also confirms that the requirement for maximum CP transmission is met by this choice of dimensions for the unit-cell since x- and y-directed transmission coefficients are equal and maximized while they have 180 degree phase difference. As promised by equations, the CP insertion loss with best value of 0.48 dB at 20.7 GHz and 2 dB bandwidth of %7.6 is achieved.

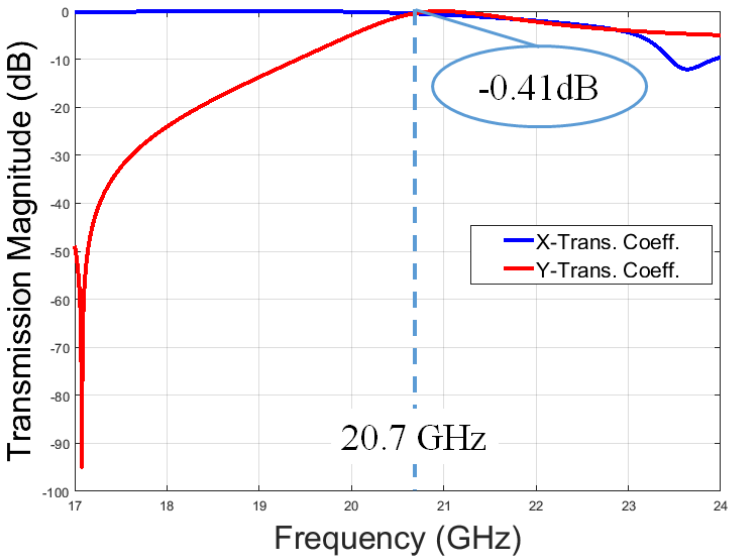

(a)

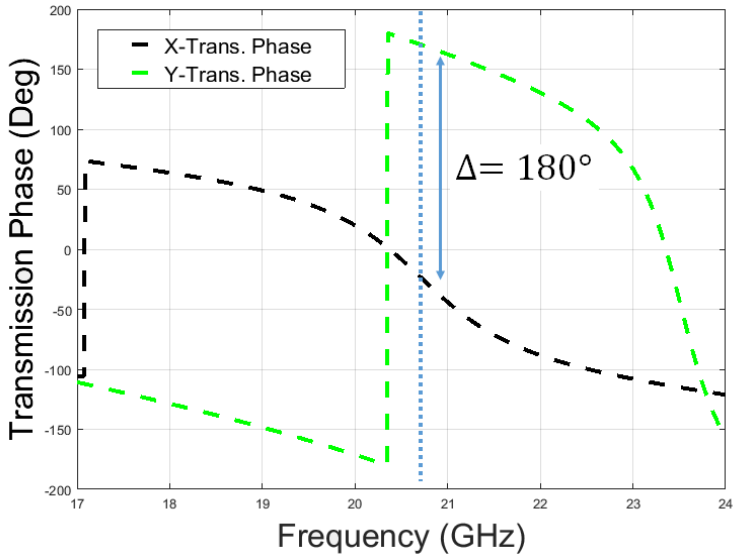

(b)

Figure 2.11 (a) Magnitude and (b) phase of the two orthogonal linear transmission coefficients.

Figure 2.1212 shows all the CP reflection and transmission coefficients. The cross-polarization level is -20dB at 20.7 GHz and 3dB AR bandwidth is %3.7. As explained in Section 2.1, the relation between transmission phase and cell rotation angle is linear at the frequency that co-polarized transmission coefficient is close to zero. Thus, cell is rotated at 20.7GHz. The transmission phase versus rotation angle is shown in **Error! Reference source not found.**13 (a).

t is transparent that transmission phase shift up to 360˚ is obtainable by rotating the unit-cell up to 180˚. Moreover, based on the definition given in [53], the element bandwidth is 19.42-21.66 GHz. The lower and upper sides of this bandwidth are where the phase varies from the nominal frequency (e.g. 20.7 GHz) no more than 45˚, for any value of the rotation angle (**Error! eference source not found.**13 (b)). The insertion loss is better than 3dB in this band.

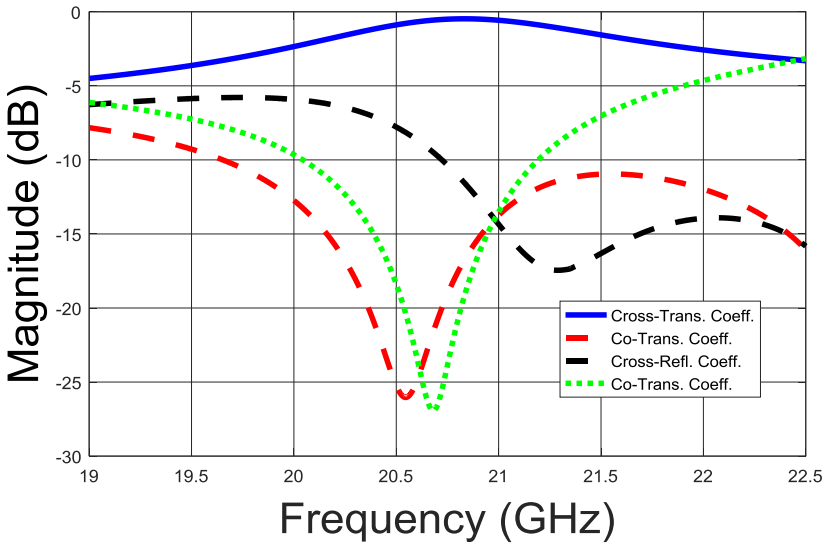

Figure 2.12 CP transmission and reflection coefficients.

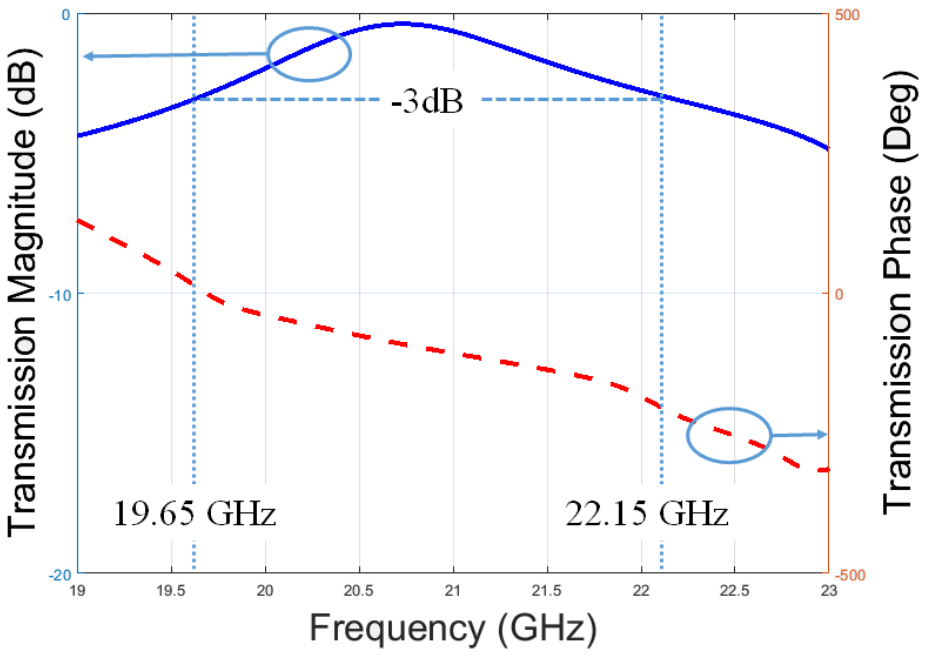

(a)

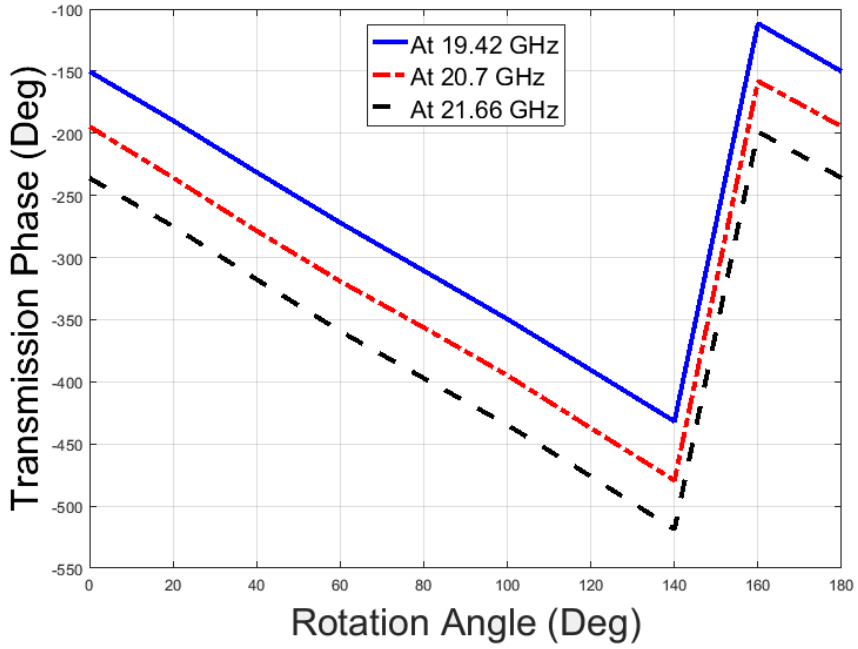

(b)

Figure 2.13(a) Cross-CP transmission magnitude and phase over frequency and (b) the transmission phase at different frequencies over rotation angle to evaluate the element bandwidth.

It is worth noticing that the dielectric loss is majorly responsible for the transmission loss of the cell. For FSS structures operating at microwave frequencies due to the excitation method, by plane waves, the dominant loss is only the dielectric loss [54]. Authors of [54] show that in the FSS structures operating at frequencies with wavelength longer than $1\mu m$, the metal roughness effect and ohmic loss are quite small and negligible. In Figure 2.14, we confirmed that the metal roughness has a negligible effect on the transmission loss. In order to account for metal roughness, one can easily choose the material type of the metallic layers as "corrugated wall" [55]. By changing the gap width, tooth width, and the depth, the amount of metal roughness can be set.

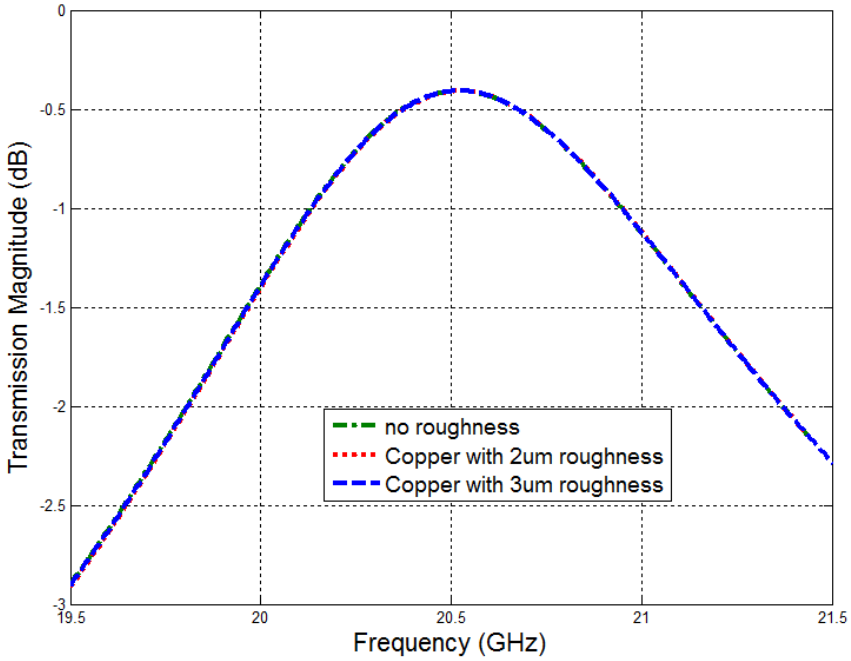

Figure 2.14 The effect of metal roughness on the transmission coefficient.

Looking at Figure 2.155, since the insertion loss does not increase to more than 3dB for

incidence angles up to 60 degrees, this unit-cell can be employed in TA systems with wide range of focal length to array dimension (e.g. F/D) ratio. All these simulations agree that the proposed unit-cell can be structured in either uniform configuration of FSS or non-uniform configuration of a TA to switch the sense of the circular polarization or converge the transmitted power to a specific direction with more gain and opposite circular polarization, respectively. Moreover, the bandwidth of this unit-cell can be improved by adding resonators to the middle layer so that the order of the equivalent filters increase.

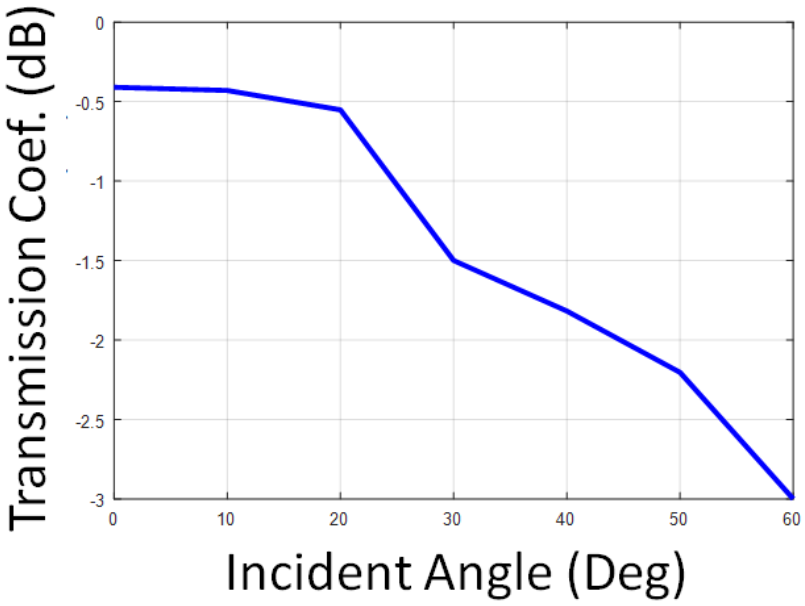

Figure 2.15 Cross- CP transmission magnitude vs different incident angles.

2.2.2 Transmit-array Configurations

As mentioned before, waves illuminating a TA surface propagates different path lengths. Consequently, they experience different phase delays. This case is illustrated in Figure 2.166. A TA focuses the feed antenna radiation to a specific direction by phase correcting these incident waves at each cell. The phase correction required to focus the radiation from a source antenna which is illuminating the center of the TA, to a desired direction can be calculated by [22]:

$$\varphi_{m,n} = \frac{1}{2}\left[k\left\{\left(r_{m,n} - r_0\right) - x_m \sin(\theta_d)\right\}\right] \quad (2.15)$$

where θ_d is the pencil beam desired direction and $\frac{1}{2}$ factor is due to the ratio of the unit-cell rotation angle to transmission phase given in (2.14), and

$$r_{m,n} = \sqrt{x_m^2 + y_n^2 + r_0^2} \quad (2.16).$$

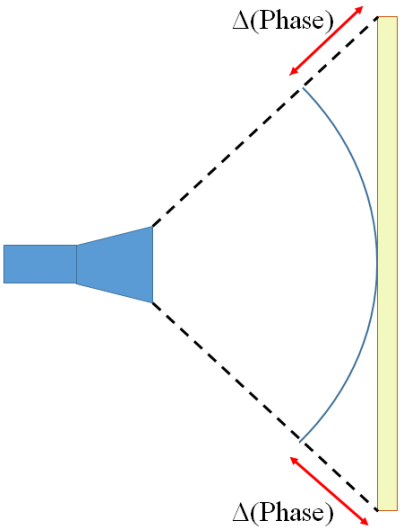

Figure 2.16 Demonstration of TA elements receiving waves with different phase delays.

Based on (2.15), two different phase distributions across the TA surface are calculated and applied to transmit broadside and -15˚-tilted beams at 20.5 GHz. Figure 2.177 illustrates these

phase distributions. This figure shows that steering the beam can also be achieved by changing the location of the feed antenna along x- or y-axis. [31] employs this method and implements a reconfigurable TA system.

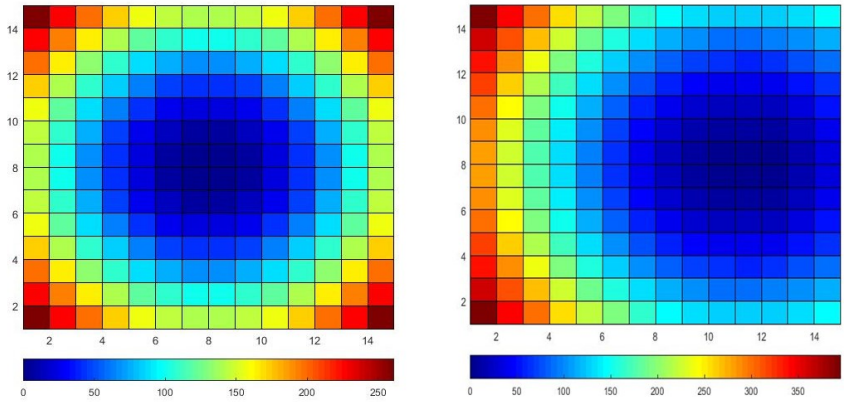

(a) (b)

Figure 2.17 Required phase distributions on TA surface for (a) broadside and (b) -15˚-tilted.

2.2.3 Feed Antenna

To test the performance of each TA, we used narrow-band 2×2 arrays of sequentially rotated CP patches (ASRP). The structure of these feed antennas is depicted in Figure 2.188. This feed system is chosen due to its similar pattern to a typical horn antenna. We compared these two feed systems regarding their radiation patterns and phase responses versus elevation angle in Figure 2.199. It should be noticed that the feed antenna's traits has great impact on the total performance of the system. These characteristics such as broadside gain, AR, and taper loss were designed carefully for our application. We designed two ASRPs operating at 20.5 GHz and 21.5 GHz with almost the same aforementioned characteristics. Figure 2.2020 illustrates the performance of the feed antenna operating at 20.5 GHz. Since the focal distance to TA side

dimension ratio is 0.8, the highest incidence angle reached for the unit-cells located at the center of the array edges will be 32°. AR and RHCP gain at this angle are 2.5dB and 2.8dB, respectively. RHCP gain at broadside is 13.1dB which means the gain drops 11.7dB at taper angle. This feature increases the spillover efficiency of the system.

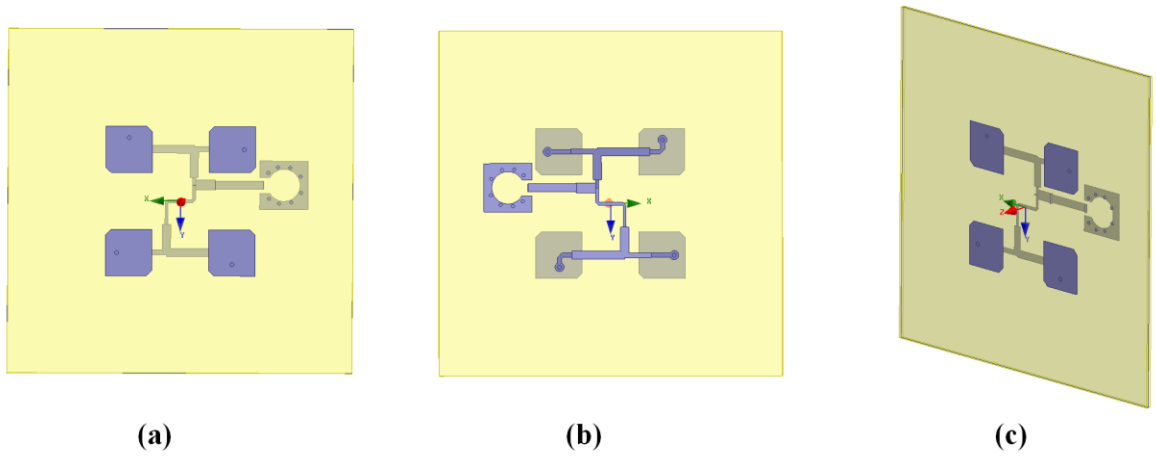

Figure 2.18 ASRP feed antenna structure: (a) top view, (b) bottom view, and (c) 3D view.

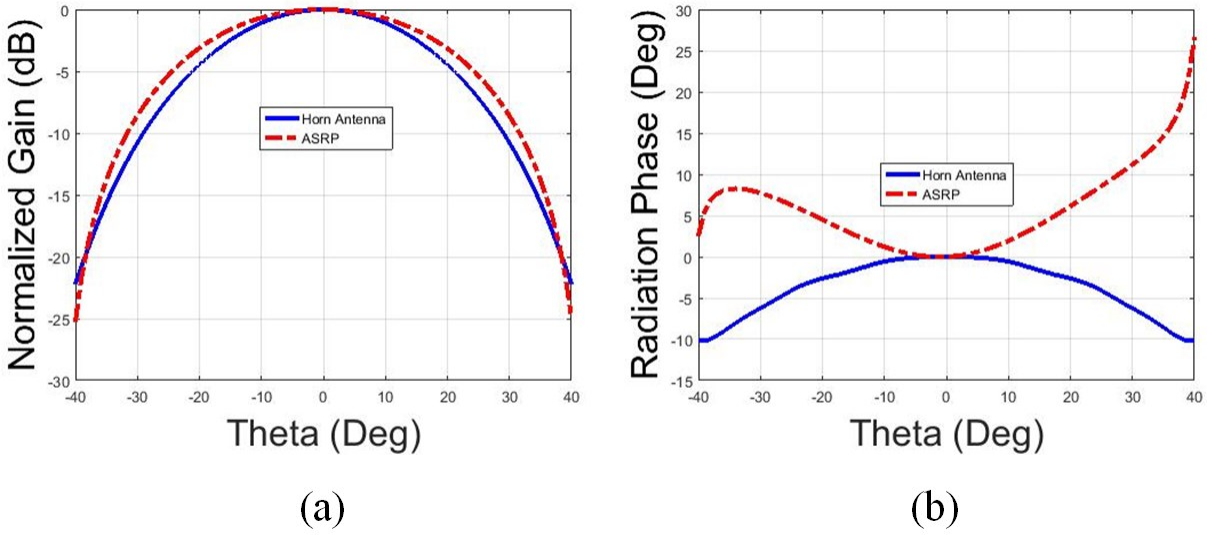

Figure 2.19 Comparison between horn antenna and ASRP antenna in (a) normalized gain and (b) phase response versus elevation angle.

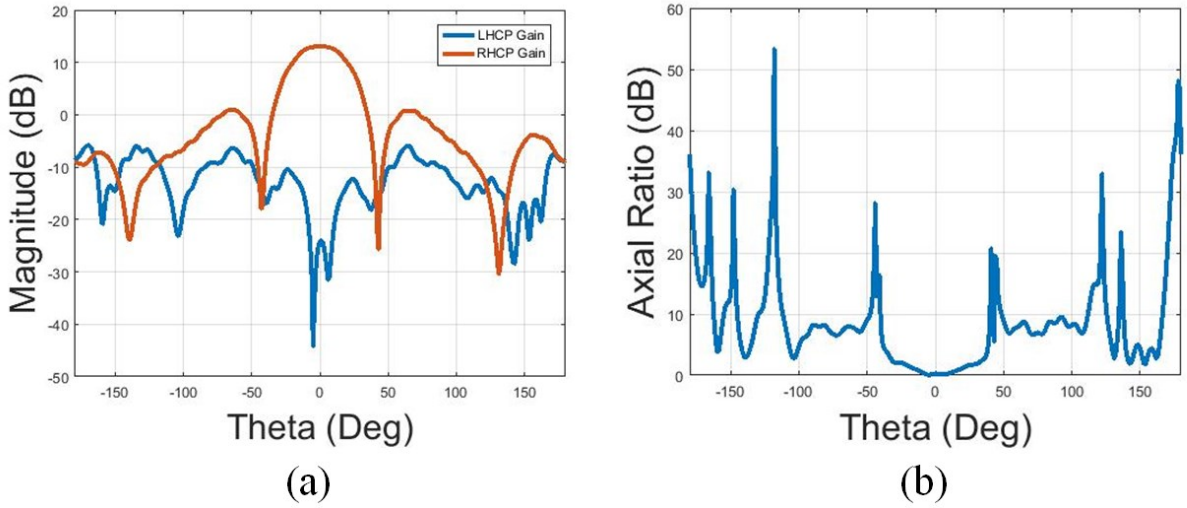

Figure 2.20 Simulated (a) CP gains and (b) axial ratio of ASRP antenna operating at 20.5GHz.

Figure 2.21 and Figure 2.22 illustrates the performance of the designed feed antennas operating at 20.5GHz and 21.5GHz over frequency, respectively. As it can be seen from Figure 2.21, the ASPR which operates at 20.5GHz has reflection bandwidth of 2.3GHz (19.7GHz-22GHz) around 20.5GHz. Moreover, the AR of the CP radiation maintains less than 2dB from 20.1GHz to 20.7GHz (See Figure 2.21 (b)). One the other hand, Figure 20.22 shows that the reflection bandwidth of the ASPR operating at 21.5GHz is 1.5GHz (20.6GHz-22.1GHz) around 21.5GHz. The AR of this feed antenna's CP radiation is below 2dB from 20.9GHz to 21.6GHz (See Figure 2.22 (b)). These characteristics guarantee that the designed feed antennas are suitable to test the performance of the TA at 20.5 GHz and 21.5GHz.

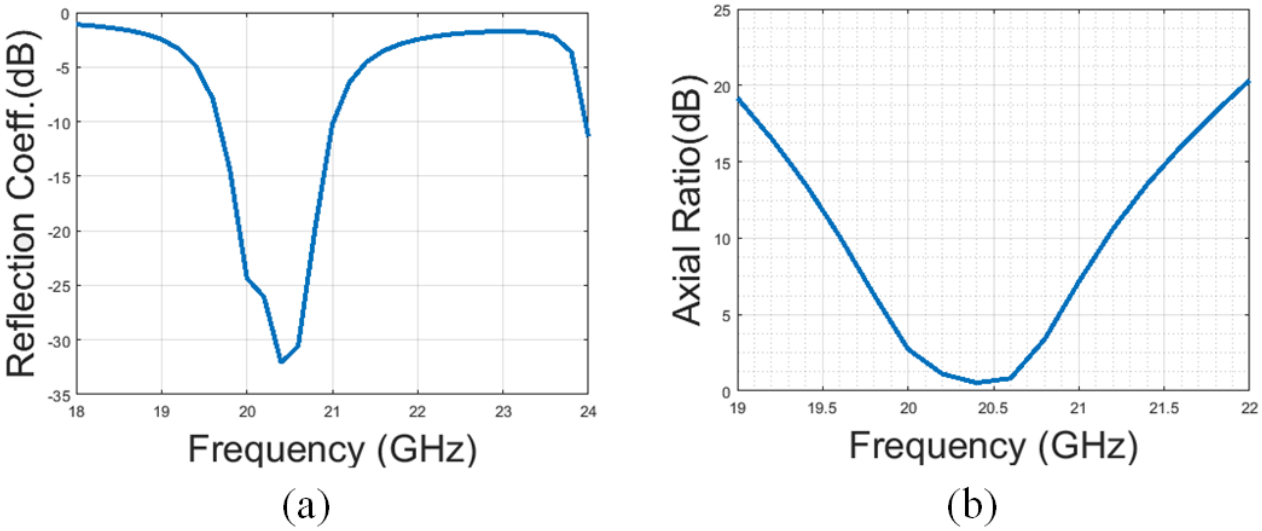

Figure 2.21 Simulated (a) reflection coefficient and (b) axial ratio of the designed feed antenna operating at 20.5GHz.

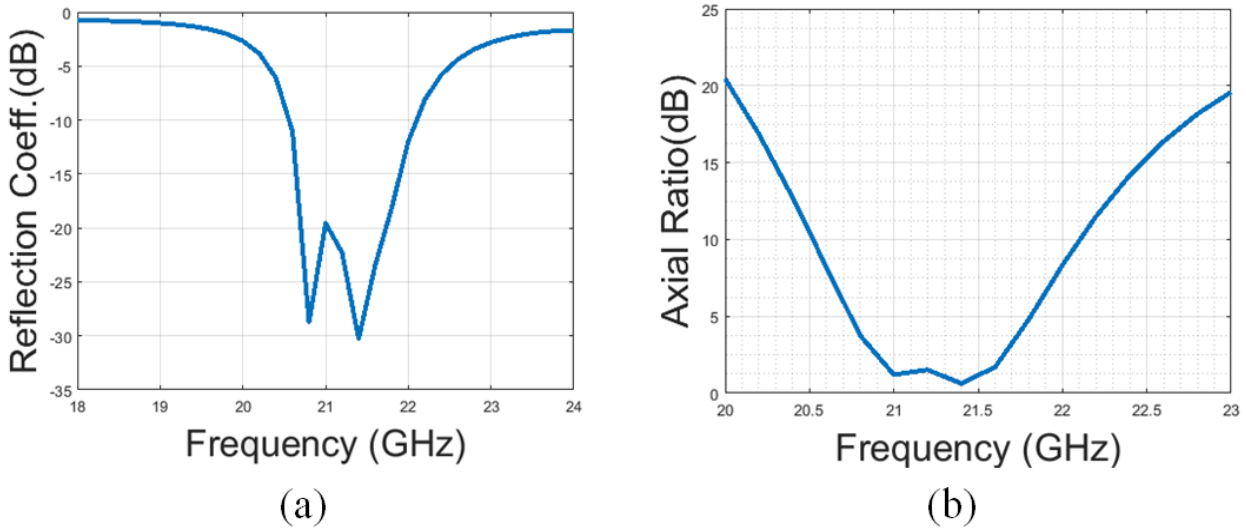

Figure 2.22 (a) Reflection coefficient and (b) axial ratio of the designed feed antenna operating at 21.5GHz.

2.2.4 Transmit-Array System

As the last step, each TA is combined with a feed antenna. This combination is illustrated in Figure 2.1. Here, we place the feed in a way that it illuminates the center of the square TA. Then,

we place the TA in front of the focal source so that $^{F}/_{D}$ ratio of the complete antenna is equal to 0.8. $^{F}/_{D}$ is defined as the ratio between focal distance (F), which is the distance between the array and the focal source, and array side diameter (D). It is worth explaining the reason we chose this ratio.

The $^{F}/_{D}$ parameter is typically chosen to be in the range of 0.5–1 [20-22]. This ratio is a substantial design parameter since it determines the total volume of the TA antenna and plays a key role for the integration and mounting of the antenna on the host platform (vehicle, building, aircraft, etc.). For example, previous implementations in X-band required an $^{F}/_{D}$ ratio of about 0.7 (21cm) for a 23-dBi antenna gain [56], when integration on vehicles (train, bus, truck, and car) would demand a thickness not larger than 10cm for SATCOM applications. Furthermore, V-band TAs with $F = 25\text{mm}$ [16] were demonstrated and could be exploited for high-data-rate communications while a low-profile solution (< 10mm at least) is required for integration in laptop or other portable devices [57].

Moreover, $^{F}/_{D}$ is an important factor that affects spillover and taper efficiencies. Spillover efficiency is the ratio of the total power illuminating the TA array and the total power radiated by the focal feed. Taper efficiency or illumination efficiency [58] determines the reduction in gain and directivity due to non-uniform fields on the radiating aperture, e. g. transmitting surface of TA. As $^{F}/_{D}$ ratio increases from 0.5 to 1, the spillover efficiency descends while illumination efficiency ascends. TA aperture efficiency which is the product of spillover and illumination efficiencies, has a pick for $^{F}/_{D}$ in range of $0.7 - 0.8$. Consequently, we fixed this ratio to 0.8 for an acceptable trade-off between spillover and taper efficiency.

We performed a full-wave simulation on the combination of TA system including feed antenna and TA at 20.5GHz and 21.5GHz for 1GHz-band each. As mentioned earlier, the TA was placed in front of two feed antennas operating at different but close frequencies to be tested. Therefore, it is explicit that the performance of TA system descends at the lower and upper sidebands of ASRP feed antennas. The convergence level for the simulations of this chapter was set to achieve errors less than 0.01 in the magnitude and 2.5˚ in the phase of S-parameters. This level of convergence was also set to be met for two consequence iterations to avoid coincident convergence. Moreover, for accurate simulations, we applied local meshing on each metallic layer of the transmit-array so that the smallest dimension of cell be divided to three mesh cells.

2.2.5 Transmit-Array System's Measurement Results

In order to measure different characteristics of the designed TA, we fabricated the two aforementioned ASPRs operating at 20.5 GHz and 21.5 GHz. Figure 2.2323 shows the fabricated prototype of this feed antenna. To feed the ASPRs, we soldered a 50 ohm surface mount connector which could operate up to 40GHz from Molex Microwave. The return loss of this SMP connector is more than 17dB in the frequency range of 12 to 40GHz. The insertion loss is about 0.22dB at 20GHz according to the product's datasheet. We used this connector plus an SMA to SMP adaptor which could also work up to 40 GHz with return loss more than 26dB in the frequency range of 12GHz to 26.5GHz. The insertion loss of only the adaptor is 0.22dB (=0.05√frequency (GHz)) at 20GHz according to the product's data sheet. Moreover, the two TAs for broadside and tilted radiation were also fabricated.

At the beginning, we measured the reflection coefficients of the feed antennas using Agilent vector network analyzer (VNA). We calibrated the VNA with Agilent 85052D 3.5 mm kit

applicable for 18 GHz to 26.5 GHz. Henceforth, the broadside TA was placed at focal distance from each feed antenna to measure the whole system's reflection coefficient. The results of both steps are demonstrated in Figure 2.2424. These results prove that TA does not block any signal from the feed system and it transmits the radiation to the other side.

Thereupon, the whole system was installed in Anechoic Chamber to measure the radiation patterns of each feed antenna and TA combination. WR42 waveguide was chosen as the probe which also operates at 18 GHz to 26.5 GHz. Figure 2.2525 shows the measurement setup. To measure the CP radiation of the TA antenna, we use both horizontal and vertical LP incident waves of the probe. The measurement results of the two TAs are presented in the two following subsections.

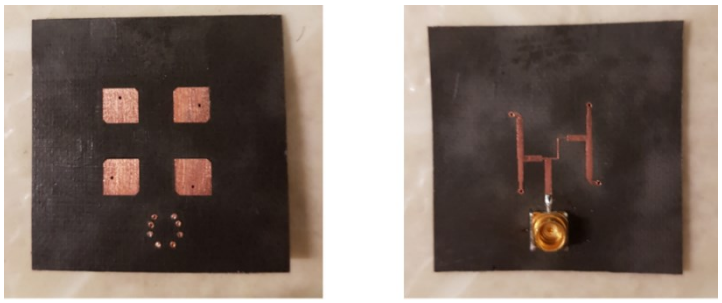

(a) (b)

Figure 2.23 (a) top view and (b) bottom view of fabricated ASRP.

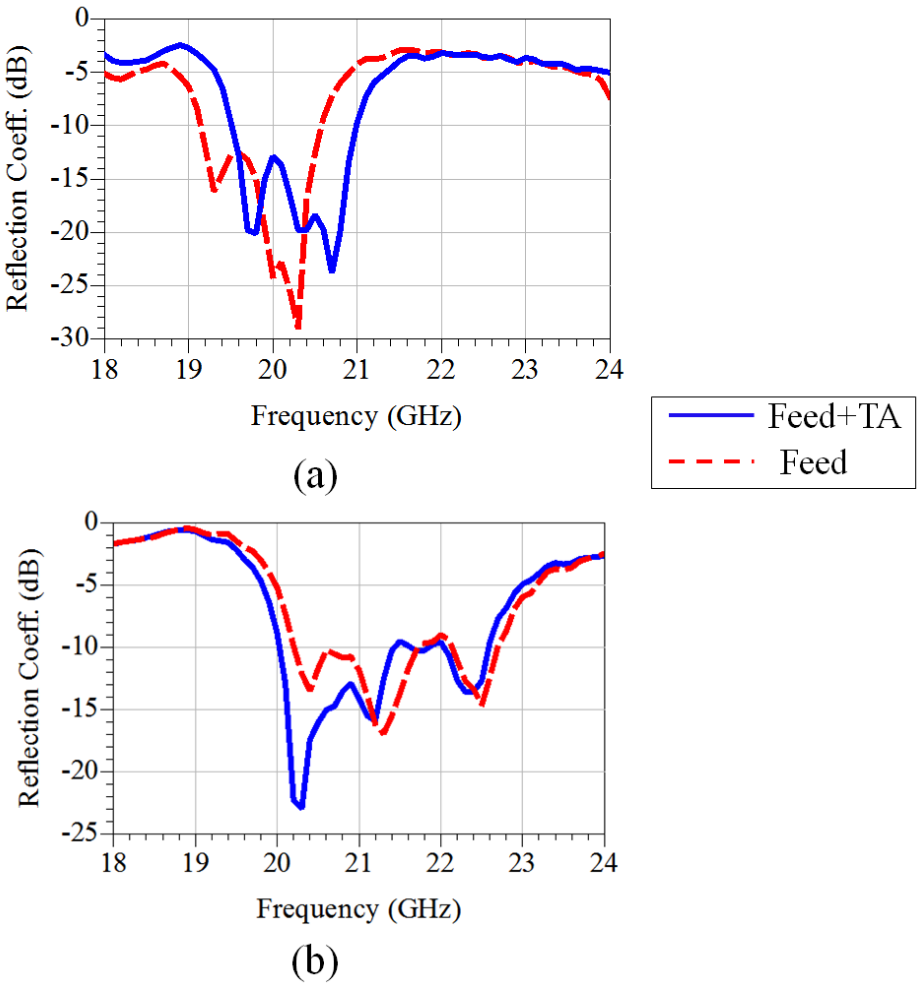

Figure 2.24 Measured reflection coefficients of feed antennas operating at (a) 20.5GHz and (b) 21.5GHz and their combinations with broadside TA.

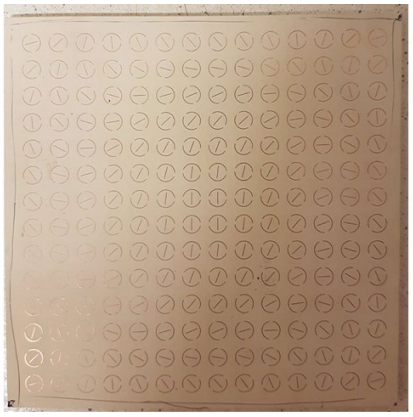

(a)

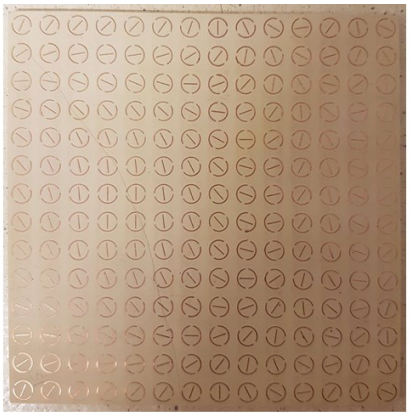

(b)

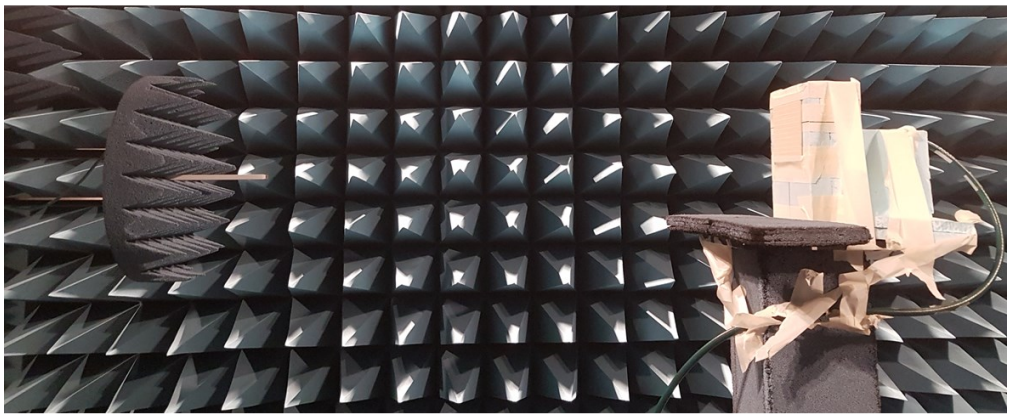

(c)

(d)

Figure 2.25 (a) Fabricated broadside TA, (b) fabricated TA for tilted radiation, (c) front view of measurement setup, and (d) side view of the measurement setup.

2.2.5.1 Broadside TA Measurements

In this subsection, the CP radiation patterns of the broadside TA in front of the two feed antennas are demonstrated. Figure 2.2626 compares the reflection coefficient of the feed antenna alone with the TA antenna as well as the simulated reflection coefficient of the TA antenna with the measured one. The coupling between the TA and the ASPR leads to a frequency shift in the reflection coefficient of feed alone. In the simulated model, we only considered the SMP connector with a perfect waveguide excitation as shown in Figure 2.1. Modeling the SMP to SMA adapter and the coaxial connector of the Vector Network Analyzer (VNA) would increase the required time of simulations and make it difficult to optimize. Therefore, we can see in Figure 2.26, the presence of the SMP to SMA adaptor and the coaxial cable of the VNA might have affected the radiation of the narrowband feed antenna and shifted the frequency response of the whole structure.

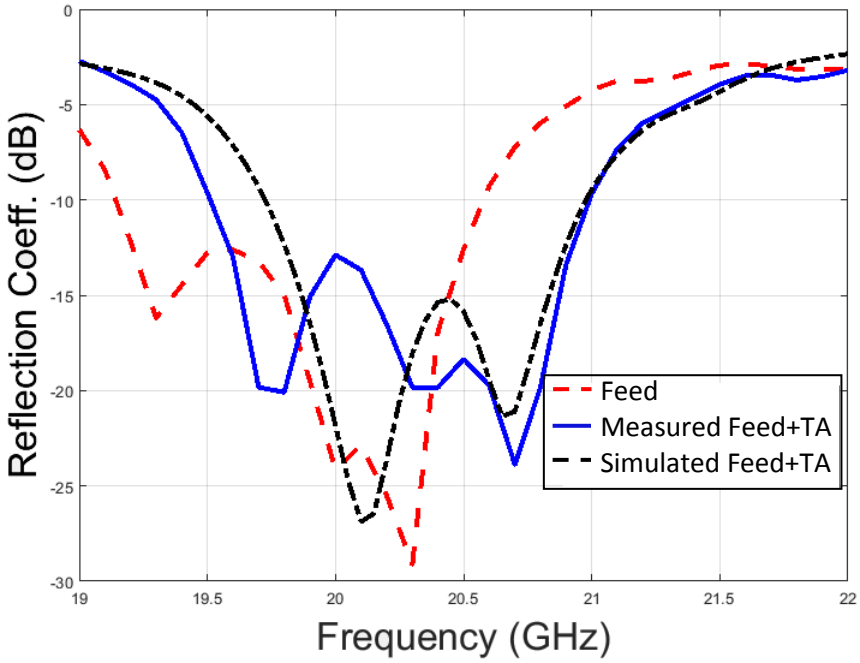

Figure 2.26 Simulated and measured reflection coefficients of the first feed alone and the TA antenna.

Figure 2.277 shows the radiation patterns of the ASPR operating at 20.5 GHz and the first TA in front of it at 20.5GHz. It can be seen that the radiation pattern of ASPR is directed to broadside with 40˚ 3dB-beamwidth whereas the TA antenna's radiation pattern is directed to broadside with 10˚ 3dB-beamwidth. Therefore, the beamwidth of the antenna combined with the TA is much narrower than the beamwidth of the antenna alone which indicates the increase in the gain of the antenna. The maximum measured gain of the feed antenna at 20.5GHz is 12dB. The maximum simulated LHCP gain of the broadside TA antenna is 23dB at 20.5 GHz while the maximum measured gain is 22.5dB at the same frequency which can be because of fabrication errors and setup inaccuracies in the chamber. Therefore, the TA increased the feed's gain with 10.5dB.

Figure 2.288 compares the measurement and simulation results of normalized RHCP and LHCP radiations of TA antenna. There is a large difference between the level of simulated RHCP pattern and measured RHCP pattern at broadside which stems from inaccuracy of feed antenna's fabrication. Basically, greater magnitude of fabricated ASPR's AR at broadside in comparison with the simulated one leads to higher AR in the TA antenna. Figure 2.299 compares the radiations of the feed antenna operating at 21.5GHz and the broadside TA antenna at 21.5GHz. As it can be seen, the TA still functions to increase the gain of the feed antenna by narrowing the beamwidth. Figure 2.3030 shows the normalized simulated and measured LHCP and RHCP radiation patterns of the feed antenna operating at 21.5GHz. The AR is 2.22dB at broadside at 21.5GHz and the maximum measured gain is 22.5dB.

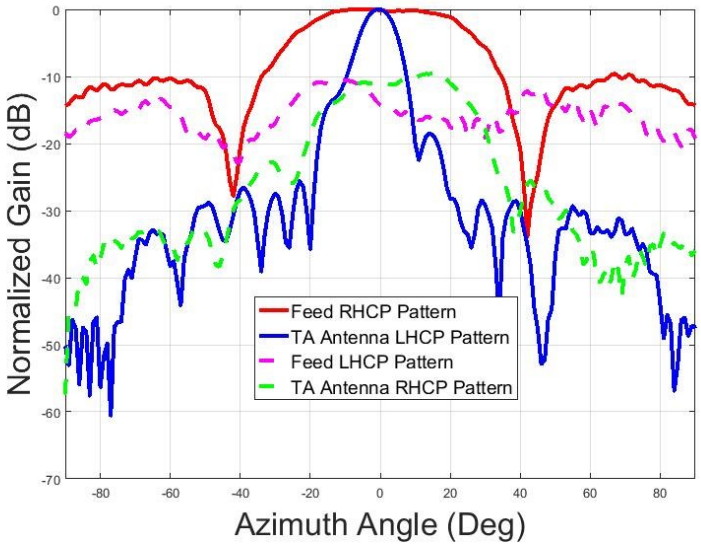

Figure 2.27 Measured normalized radiation of ASPR and TA antenna at 20.5 GHz.

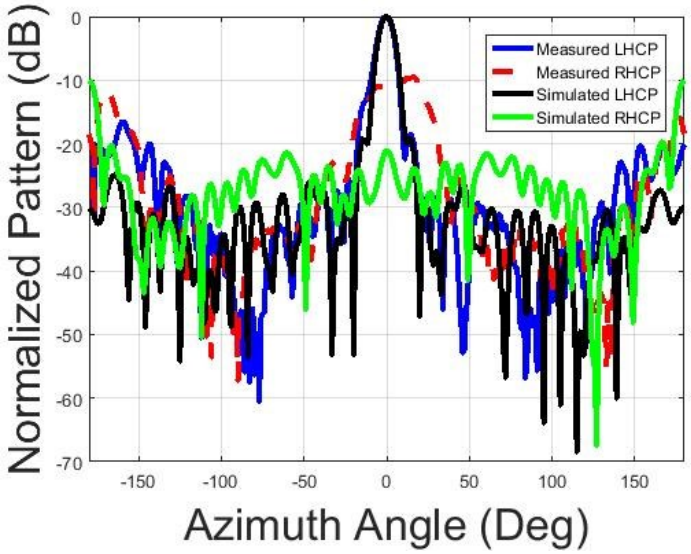

Figure 2.28 Measured and simulated RHCP and LHCP radiation patterns at 20.5 GHz.

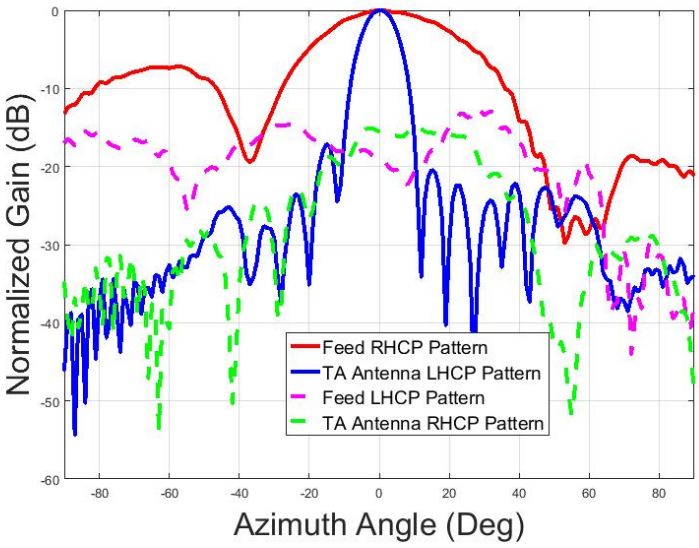

Figure 2.29 Measured normalized radiation of ASPR and TA antenna at 21.5 GHz.

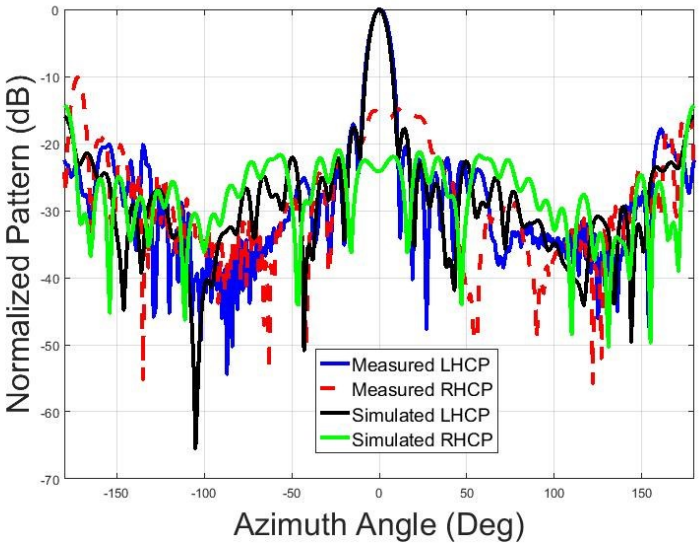

Figure 2.30 Measured and simulated RHCP and LHCP radiation patterns at 21.5 GHz.

Loss budget and aperture efficiency of the broadside TA system at 20.5 GHz is summarized in Table *2.2*. The efficiencies are calculated from simulation results and they are based on the following equations [59, p. 138].

$$spillover\ efficiency = \frac{\int_S R(x,y)\,dxdy}{\int_{4\pi} R(\theta,\varphi)d\Omega} \qquad (2.17)$$

, where $R(\theta,\varphi)$ is the radiation pattern of the feed antenna and S presents the whole surface of the TA. Therefore, the spillover efficiency measures the ratio of the power intercepted by the transmitting elements to the total radiated power by the focal source. The spillover efficiency can be escalated by either placing the TA closer to the feed or increasing the size of the TA.

$$taper\ efficiency = \frac{1}{S}\frac{\left[\int_S |\vec{E}_a(x,y)|ds\right]^2}{\int_S |\vec{E}_a(x,y)|^2 ds} \qquad (2.18)$$

, where $\vec{E}_a$ is the vector of the electric field across the TA's aperture. Taper efficiency is a measure that how uniform the magnitude of the electric field is across the illuminating aperture. Since the aperture fields tend to fade away from the center of the TA, the gain will be lower than its maximum value. This efficiency can be improved by increasing the F/D ratio. However, there is a trade-off that increasing the F/D ratio reduces the spillover efficiency. We chose the $F/D = 0.8$ as an acceptable trade-off between spillover efficiency (2.75dB) and taper efficiency (3.3dB).

Table 2.2

TA System Efficiency

Efficiency Type	**Loss (dB)**
Taper	3.3
spillover	2.75

2.2.5.2 Tilted TA Measurements

We placed the TA with asymmetric phase distribution across it in front of the ASPR operating at 20.5GHz. The TA is designed to increase the directivity of feed antenna's radiation while redirecting it to -15˚-off broadside. Figure 2.3131 presents the measured radiation patterns of the feed antenna and the TA antenna at 20.5GHz. It can be seen that the radiation pattern of ASPR is directed to broadside with 40˚ 3dB-beamwidth whereas the TA antenna's radiation pattern is directed to -17˚ off broadside with 11˚ 3dB-beamwidth. Therefore, the beamwidth of the antenna combined with the TA is much narrower than the beamwidth of the antenna alone which indicates the increase in the gain of the antenna. Extra tilting is caused by the misalignment errors.

In Figure 2.3232, the normalized simulation and measurement results of the RHCP and LHCP radiation patterns are demonstrated. The maximum simulated LHCP gain of TA antenna is 22.5dB at 20.5 GHz while the maximum measured gain is 21.5dB at the same frequency which can be because of fabrication errors and setup inaccuracies in the chamber. Finally, Figure 2.3333 presents the AR of the TA antenna. It can be seen that the measured AR of the TA antenna stays better than 3dB over 20GHz-21GHz at $\theta = -17^{\circ}$.

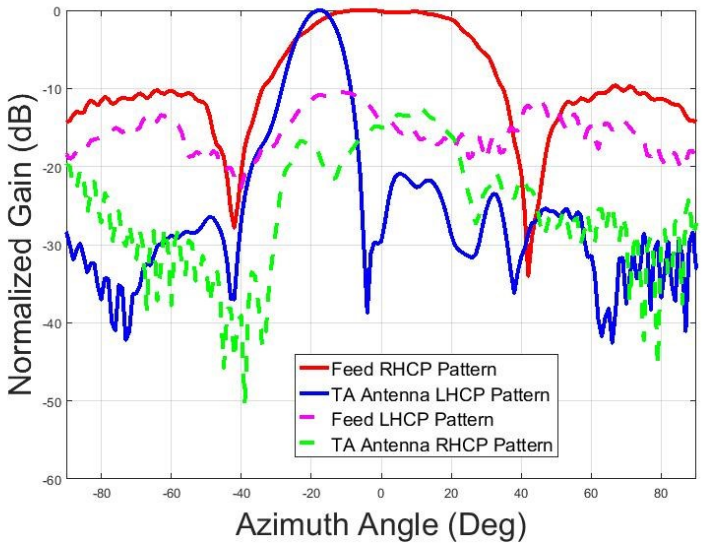

Figure 2.31 Measured normalized radiation of ASPR and TA antenna at 20.5 GHz.

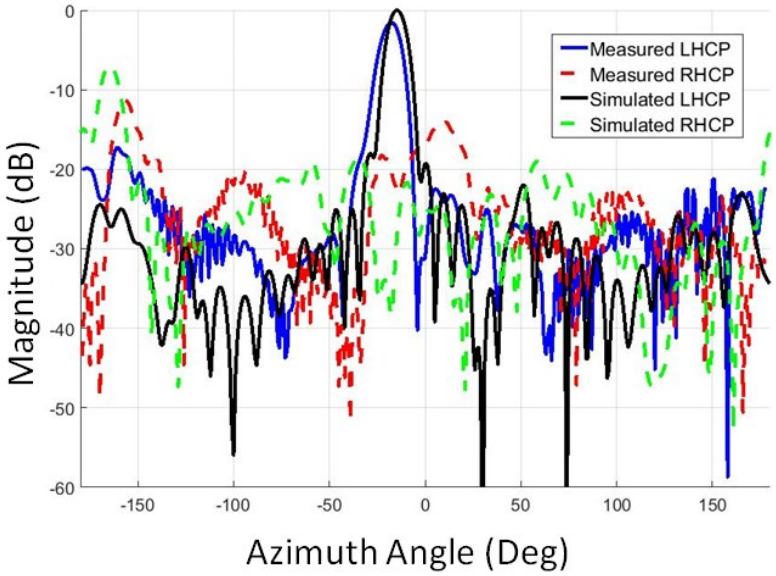

Figure 2.32 Measured and simulated RHCP and LHCP radiation patterns at 20.5 GHz.

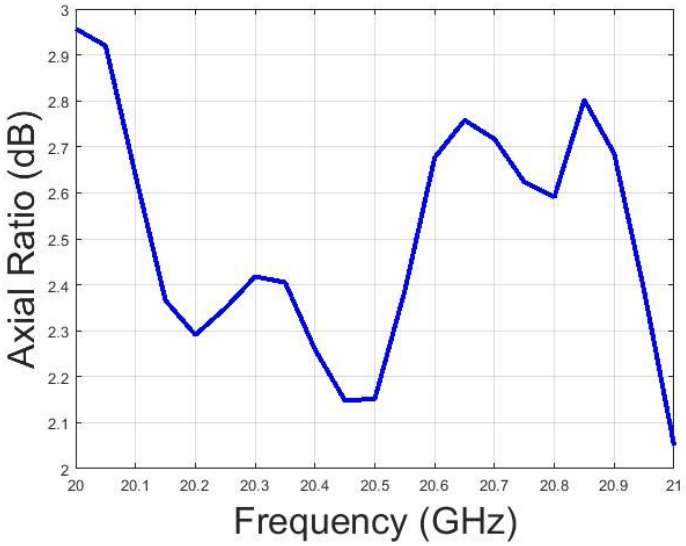

Figure 2.33 Measured axial ratio over frequencies in the direction of maximum gain (i.e. -17˚).

Although we did our best to comprise between simulation time and accuracy and make the fabricated setup as close as possible to the simulated case, there are some discrepancies between the simulation results and measurement results. In the following the probable causes of these differences are explained:

- Fabrication inaccuracies: since the operational frequency is close to 20GHz, the slightest change in the dimensions can alter the operational frequency of feed antennas. Also, the TA elements are functioning at their resonances and their transmission phase changes drastically regarding the frequency. Therefore, fabrication error not only can change the resonance frequency of the TA elements, it can also alter the required 180˚ phase difference between the transmission phases of the two orthogonal linear polarizations. Consequently, depending on at which element (the split ring, the grid, or both) the fabrication error might have occurred, the error can lead to higher amount of axial ratio.

- Misalignment errors in TA antenna: As shown in Figure 2.1, a feed antenna is illuminating exactly the **center** of a transmit-array which is **parallel** to the surface of the feed antenna. A robust setup to hold and fix the distance between the feed and the transmit-array like a 3D printed holder could reduce a probable error in this setup. However, printing such setup was time consuming and it was also out of the scope of this thesis. So, we made a setup from foams to hold the two antennas. Although we did our best to accurately mimic all the dimensions from the simulations, any tilt and any shift offsetting the centers of the two parallel planes holding the feed antenna and the TA could lead to an extra tilt in the radiation patterns.
- Misalignment error in measurements: Before starting the measurements, the antenna aperture has to be aligned with the probe aperture which is a Standard Waveguide. Since the antenna is small and fragile and it is fixed on its rigid coaxial cable, the alignment is done visually as:

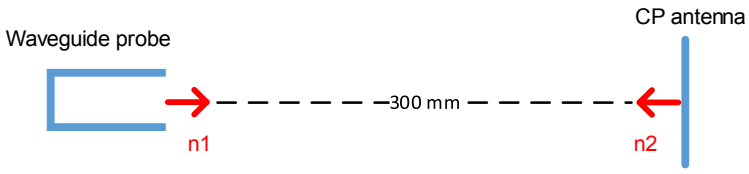

Figure 2.34 Virtual alignment line in measurement setup.

The vectors n1 and n2 are unit vectors perpendicular to probe and antenna aperture and at the center of the aperture. To have a correct measurement, n1 and n2 vectors should be along the same line. Considering the 70 cm distance between them (this is the closest distance we could put the antenna and the probe in the anechoic chamber), this is a difficult task. There is always an unavoidable error associated with this process. A typical alignment error is shown here:

Figure 2.35 demonstration of how misalignment error can happen in measurement setup.

Unlike the linearly polarized antennas, to measure the CP fields, both E_x and E_y amplitude and phase have to be measured. This makes the measurements more sensitive to alignment.

2.3 Same Sense Bidirectional CP Antenna

Bidirectional CP slot antennas naturally radiate opposite sense of CP signals on their two sides [21]. It is already well known that the behavior of a slot antenna can be analyzed using the magnetic currents in the slot. The opposite directions of the equivalent magnetic currents on the two sides of the slot lead to opposite senses of the CP radiations from these sides. For instance, RHCP signal is radiated on the right side of the antenna while LHCP wave is radiate on the left side. This fact can introduce errors in communication systems such as GPS navigation system that considers only one sense the desirable signal [21]. Therefore, if we can convert the undesirable CP sense on one side to the opposite one, both the full radiation power of the antenna can be exploited thoroughly and the unwanted signal is eliminated. Consequently, we utilized the same unit-cell mentioned in this chapter in polarization converting FSS for this application.

To change the sense of CP polarization, the unit-cell has to transmit both x- and y-directed LP waves with the same magnitude and 180˚ phase difference. This is in fact exactly what the designed unit-cell in this chapter does. The unit-cell dimensions are scaled so that it functions at 1.72GHz. 1.72GHz was chosen as a representative of lower frequencies in order to demonstrate

the point that this unit-cell is scalable for other applications at various frequencies. The new cell's dimensions are summarized in Table 2.3. Figure 2.3636 shows the structure of this cell.

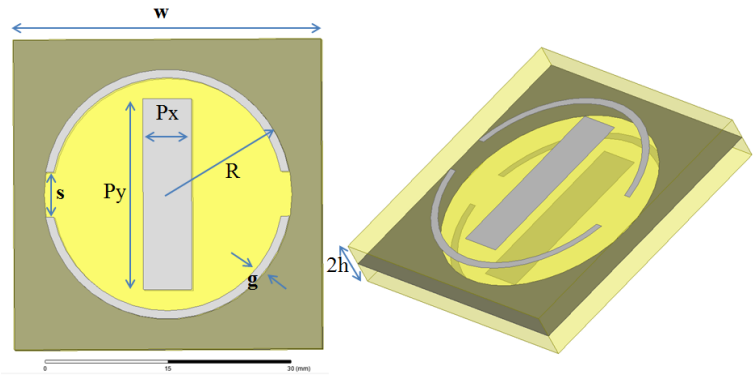

Figure 2.36 FSS unit-cell structure.

Table 2.3

FSS Unit-Cell Parameters

Parameter	w	P_x	P_y	S
Value	38 mm	6 mm	23.4 mm	5.5 mm
Parameter	g	R	H	ε_r
Value	1 mm	15.3 mm	3.175 mm	6

Hereafter, the cell is structured in a uniform 3×3 array of FSS. The FSS is placed in a close distance from the side of the slot antenna that radiates LHCP signal. The radiating antenna is an L-shaped circularly-polarized slot antenna proposed in [60]. Therefore, a same sense CP bidirectional antenna radiating RHCP signal at both sides is designed and simulated. The unit-cell's CP reflection and transmission coefficients are depicted in Figure 2.377. It can be seen that the cross-polarized transmission coefficient is maximized and the rest of the coefficients are minimized. Therefore, the polarization of the wave changes after transmission from the unit-cell.

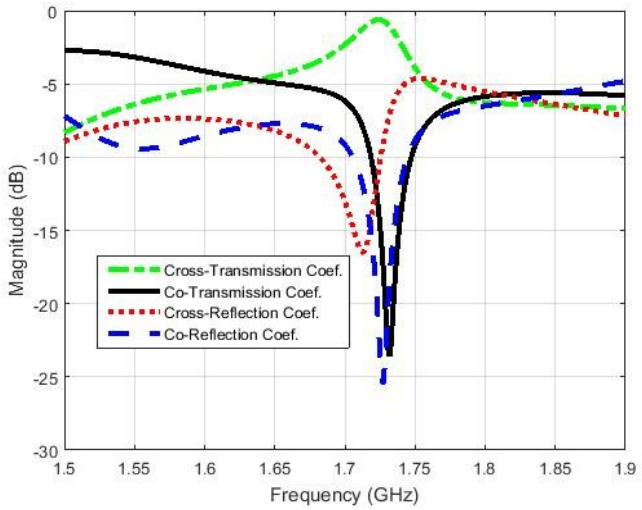

Figure 2.37 CP S-parameters of the unit-cell.

The distance between the antenna and the array is chosen to be 10 mm so that the FSS would be in near-field of the antenna and different elements on the FSS do not experience phase difference from the illumination source, e.g. CP slot antenna. The antenna and the array are both designed to operate at 1.72 GHz. However, the close distance between the antenna and the FSS causes great amount of coupling between them, which leads to some reduction in AR of the antenna compared to when it operates alone. Therefore, some optimization was done in the antenna to achieve the best performance of the whole system.

The whole antenna's performance in term of LHCP and RHCP gains is shown in Figure 2.388 (a) and it is compared with RHCP gain of slot antenna. In Figure 2.388 (b), reflection coefficient of the combined antenna is illustrated. The presented result confirms that the presence of FSS in a close distance of antenna provides right handed CP radiation on both sides of the antenna.

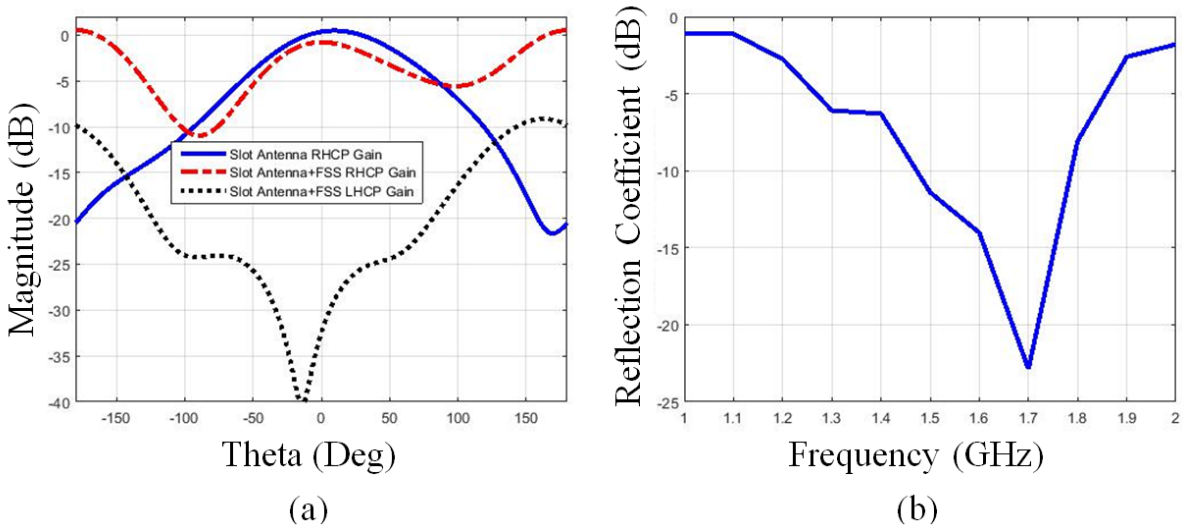

Figure 2.38 (a) LHCP and RHCP gains of slot antenna combined with FSS in comparison with RHCP gain of slot antenna and (b) reflection coefficient of slot antenna combined with FSS.

2.4 Conclusion

In this chapter, an AFA-based unit-cell using miniaturized elements is designed and simulated. The cell structure is asymmetric along x- and y-axis. This element behaves differently for x- and y-directed LP waves such that it transmits them with equal magnitude and 180˚ phase difference. Therefore, once the unit-cell is illuminated by a CP wave, it propagates the incident wave with minimum insertion loss while it changes the sense of the CP wave. The design procedure of this cell is performed in a way that a transmission phase of up to 360˚ in CP wave can be achieved by cell rotation technique.

The main purpose of designing this unit-cell is that it can be configured in a TA. Since elements on diverse parts of a TA surface receive waves with variant phase delays, they require to compensate for these phase differences while transferring the waves. Hence, the radiated power

from all elements add in a constructive manner in a specific direction. Consequently, this unit-cell with different rotation angles is configured in two different TAs installed in front of focal sources. The focal sources are 2×2 array of sequentially rotated CP patch antennas. The gain of focal sources are typically 13dB in average and they have AR less than 0.8dB at broadside. Having ideal features in the feed antenna of TA system is essential as it directly impacts the performance of the whole system.

Two feed antennas, each of which is sequentially rotated CP patch antenna, were fabricated. These antennas have narrow-band reflection and AR and they operate at 20.5 GHz and 21.5 GHz. Moreover, two TAs to radiate a directive pencil beam to broadside, 15˚ off broadside, and 30˚ off broadside were fabricated. The simulation and measurement results agree well. According to both results, the 3dB-gain bandwidth of the TA is between 19 GHz and 23 GHz (19% bandwidth). The TA also maintains AR below 3dB for radiations up to 30˚ from broadside.

Furthermore, this unit-cell has the capability to change the sense of a CP signal by transmitting it to the other side. This means that the unit-cell can be considered as a polarization convertor by introducing 180˚ phase difference between the two orthogonal LP signals embedded in a CP wave. We took advantage of this property and structured the cell in a 3×3 uniform array. The designed FSS is then placed in close proximity of a bidirectional CP slot antenna. As a result, a bidirectional CP antenna with RHCP signal radiated at both sides is simulated at 1.72GHz. The results proved that the LHCP signal at the side that FSS is placed is suppressed and converted to RHCP signal. Moreover, the reflection coefficient of the whole antenna is close to -20dB at 1.72dB.

Chapter 3

3 Dual–Band Circularly-Polarized Transmit-Array Unit-Cell

The advancement in wireless communication systems has resulted in low cost, compact size, circular polarization radiation, and multiband operation. Especially, dual-band or multiband CP antenna systems have been proposed and widespread implemented. Although plenty passive RA cells have been proposed that function at multi frequency-bands [61-62], there is no passive solution for TAs to the best of our knowledge. This fact stems from design requirements for a TA element such as obligation of impedance-matching to free-space at each desired frequency.

Here, we propose a novel unit-cell composing of miniaturized elements. The structure of this cell is depicted in Figure 3.1. This cell has three-layer AFA-based structure. Both transmitter and receiver parts compose of capacitive patches and inductive split rings. These two sides of the cell are connected through non-radiating resonant slot layer (See Figure 3.1 (b)). The proposed unit-cell has dual-band operation for CP incident waves. The required phase shift at each element is achieved by ERT at each frequency. This method, as mentioned before, provides continuous phase correction ability whereby it minimizes quantization loss. The proposed TA cell has several interesting characteristics: First, it maintains circular polarization transmission at two desirable frequencies. Secondly, unlike conventional FSS-based cells it provides up to 360˚ phase shift with only three-layer structure. Less metal layers not only simplifies the fabrication process, it also reduces the prototyping errors. Thirdly, the achievable 360˚-phase-shift. It means the final TA system suffers from less quantization loss in comparison with systems employing 1-

or 2-bit phase shifters. Last but not the least, the final system can be mechanically re-configurable and steer different angles.

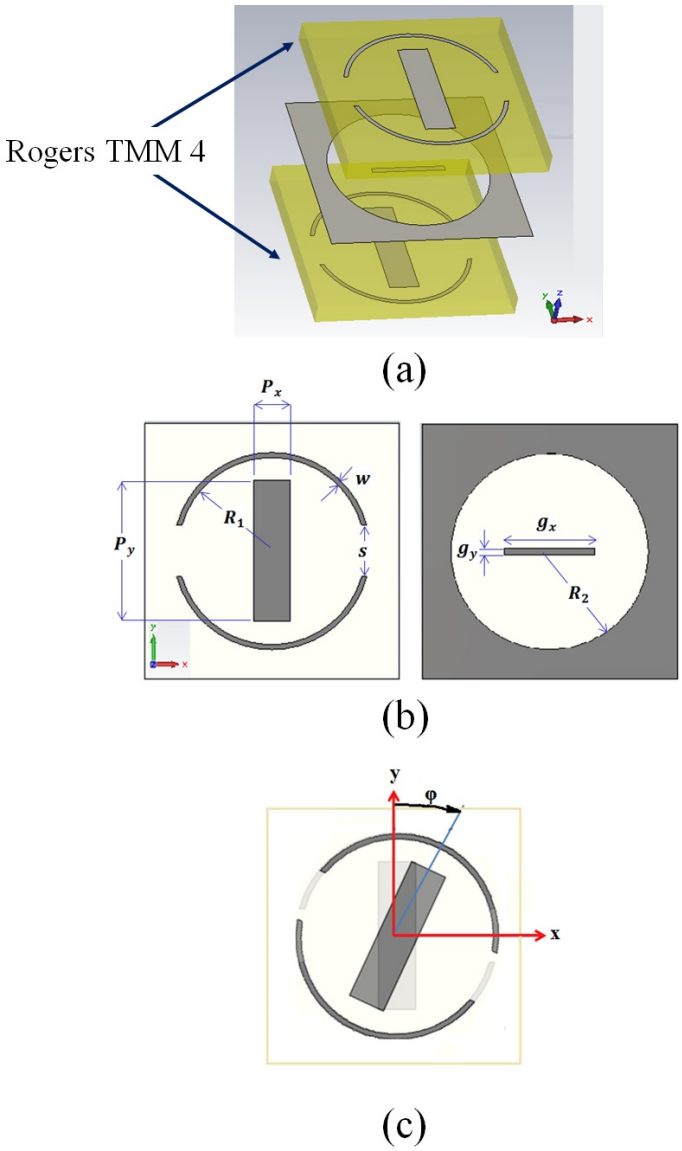

Figure 3.1 (a) Topology of the proposed TA unit-cell. (b) The unit-cells of the first and second layers at left and right respectively (c) top view of the rotated unit-cell.

This unit-cell is described in detail in the following Sections. The analysis, design procedure, simulation results, and measurement results of the unit-cell performance are also explained in sections 3.2 and 3.3, respectively.

3.1 Principle of Operation

In chapter 2, we explained how we broke down circular-polarized scattering parameters in terms of LP reflection and transmission coefficients. Here, we just repeat the design requirements resulted from equations written in chapter 2.

$$T_{cross-pol} = \frac{1}{2}(S_{21}^{xx} - S_{21}^{yy})e^{\pm 2j\varphi} \quad (3.1)$$

$$T_{co-pol} = \frac{1}{2}(S_{22}^{xx} + S_{22}^{yy}) \quad (3.2)$$

, where φ is the cell rotation angle as shown in Figure 3.1(c). It can be noted from the above equations that to obtain the required phase shift in the CP transmitted wave, the linear transmission coefficients must be maximized with equal value and 180 degrees phase difference:

$$|S_{21}^{xx}| = |S_{21}^{yy}| \quad (3.3)$$

$$\angle S_{21}^{xx} - \angle S_{21}^{yy} = \pm 180^{\circ} \quad (3.4)$$

Once these requirements are met, the transmitted wave from the unit-cell has the opposite sense of polarization from the incident wave and the reflected wave from the unit-cell is minimized. Moreover, the transmission phase is twice the amount of the physical rotation of the corresponding unit-cell. The unit-cell shown in Figure 3.1 meets these requirements and its design procedure is explained in the following sections. The structure consists of two-

dimensional periodic arrangement of capacitive patches, inductive split rings on first and third substrate layers, and the inductive grids on the middle substrate layer. For the purpose of our application, which is designing a dual-band CP TA unit-cell, the proposed structure has to behave differently for the two orthogonal components of the incident wave at two different frequencies of interest. This behavior is illustrated by modelling the proposed unit-cell as different passband filters for the two linear polarizations as shown in Figure 3.2.

Ideally, at the two different frequencies of f_1 and f_2, the equal value of S_{21}^{xx} and S_{21}^{yy} is 0 dB and the phase difference between them is 180 degrees at both frequencies. The 180˚ phase difference is achievable when the input impedance of the structure is slightly different for the x- and y-directed incident waves. The equivalent circuits of the cell when it is illuminated with each of the two orthogonal linear waves are depicted in Figure 3.3. In the proposed structure, the rectangular patch and the split ring operate as a capacitor ($C_{x,y}^1$) and an inductor ($L_{x,y}^1$) respectively.

These lumped elements are in series when the cell is illuminated by x-directed electric field while they are in parallel when y-directed electric field illuminates the cell. Figure 3.3 (a) and (b) show these equivalent circuits respectively. Their combination results in a zero in transmission and reflection coefficients respectively. Therefore, the former behaves as a band-stop filter and the latter functions as a pass-band filter. By engineering these filters, we can obtain 180˚-phase difference at two different frequencies. The circular slot and thin grid placed at the middle layer function as shunt capacitor ($C_{x,y}^2$) and inductor ($L_{x,y}^2$). The transmission lines with the characteristic impedance of Z_1 and the length of h are models of the dielectric slabs with height of h and constant permittivity of ε_r between the metal layers in the final unit-cell structure. For non-magnetic media Z_1 can be calculated by equation (3.5). Free space on each side of the device is modeled with the $Z_0 = 377\Omega$.

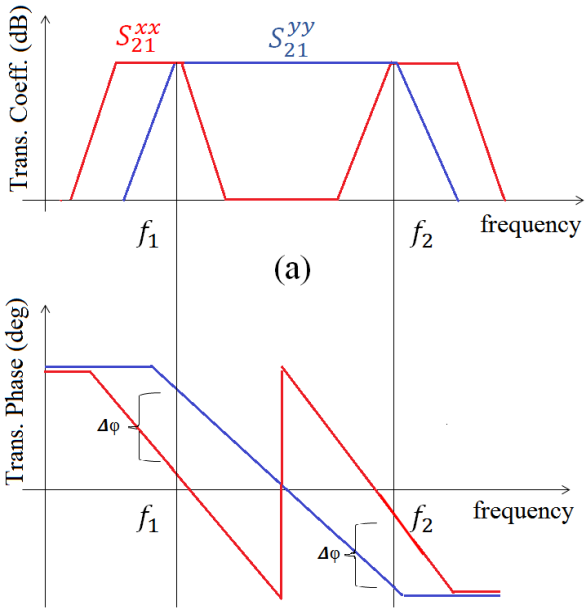

Figure 3.2 (a) Amplitude and (b) phase of desirable transfer functions to design a dual-band CP TA unit-cell.

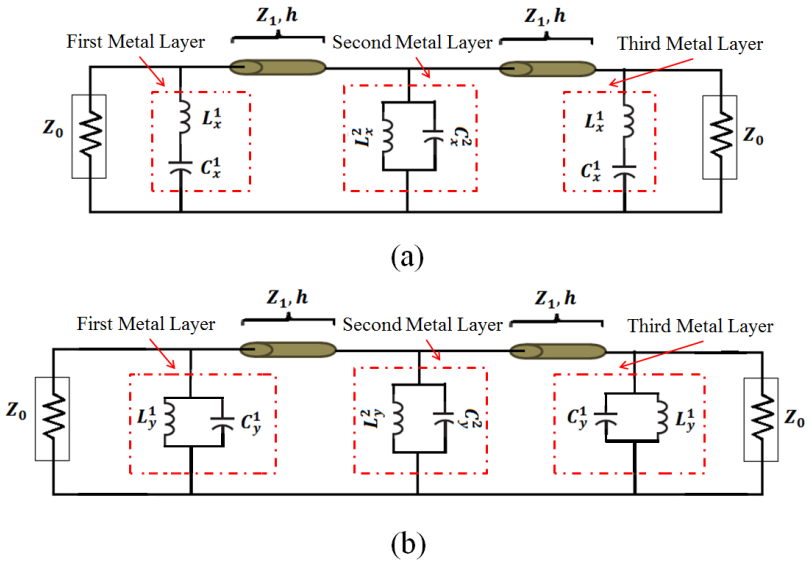

Figure 3.3 Equivalent circuits of unit-cell once it is illuminated by (a) x-directed and (b) y-directed electric fields.

3.2 A Design Example and Results

The design procedure of the proposed unit-cell is based on achieving the transmission characteristics of the required responses for both vertical and horizontal polarizations. These responses are chosen based on the operational bands of interest. For example if f1 and f2 are the desired frequencies as shown in Figure 3.3, the structure should resonate close to f1 and f2 for the two waves with slight difference in frequency. The amount of the shift in frequency from either f1 or f2 are selected in a way that the 180˚ phase difference is achieved at both frequencies, meanwhile the cross point of the two reflection coefficients has to be at their minimum possible amplitude. The reason to satisfy the latter one is that a TA unit-cell has to be impedance matched to the free space to minimize the reflection. The separation between f1 and f2 is controllable with the choice of the substrate thickness. In this paper, f1 and f2 are considered to be 10.8 GHz and 16.7 GHz respectively. The physical dimensions are summarized in Table *3.1*.

The reflection coefficients are shown in **Error! Reference source not found.**. One can discuss hat the structure of the cell presented in this chapter is very similar to the one in the second chapter and wonder what the difference is. As we showed in the second chapter the structure composed of three metallic layers can resonate in three different frequencies. While in the cell presented in the second chapter, we achieved the required criteria by applying asymmetry and grid elements to affect the second frequency of resonance, that method is not adequate here as we need to meet the same criteria at two frequencies. By comparing Figure 3.4 and Figure 3.5, one can see that the phase difference between the responses of the cell to the two orthogonal polarizations starts when the cell resonates in response to the TE incident wave (x-directed wave)

and not the TM one at 9.5GHz. Therefore, we can achieve 180˚ phase difference between the responses not only at the first desired frequency but also in a higher frequency.

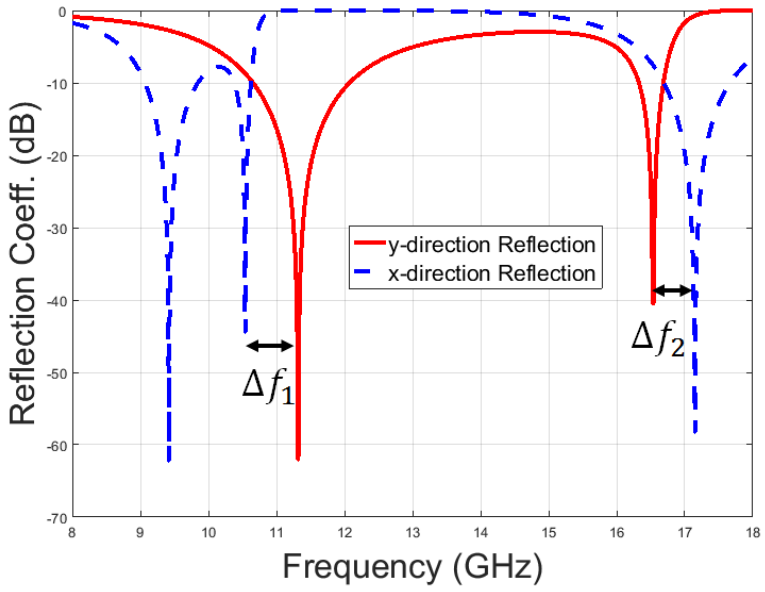

Figure 3.4 Reflection coefficients of the two orthogonal polarizations with slightly difference in resonance frequencies.

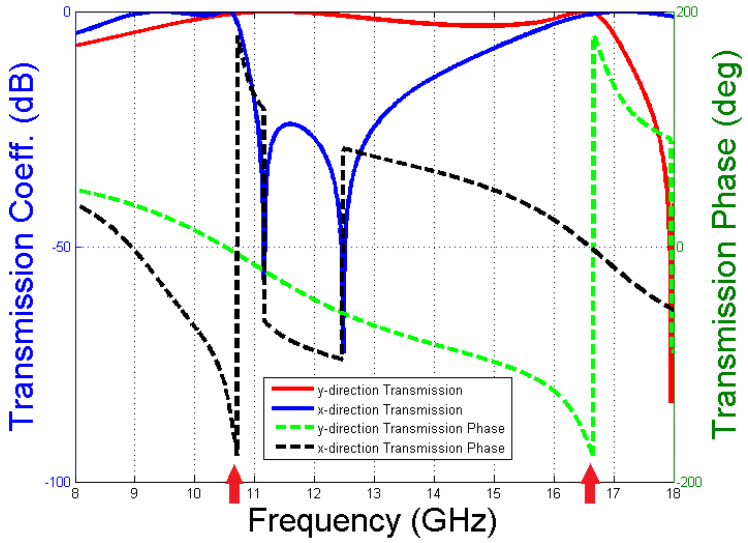

Figure 3.5 Transmission coefficients of the two orthogonal polarizations with 180° difference in phases at both 10.8 GHz and 16.7 GHz.

It is worth mentioning that the resonance frequencies at 9.5GHz and 11.3GHz in TE response and TM response, respectively, are main resonances of the elements at the first layer. However, the resonance frequency at 10.5GHz, which is the key factor in this design, is the resonance caused by the coupling and the interaction of the first layer and the third layer elements through the second layer slot. This kind of response is typical response of "doubled" resonators and it appears when the coupling between the doubled resonators is strong enough [63]. The frequency of this secondary resonance can be altered by changing the amount of coupling between the elements. For instance, here, we exploited this secondary resonance by reducing the thickness of the substrate from 1.27mm to 0.76mm in comparison with the cell presented in Chapter 2. The authors of [63] thoroughly explored this kind of response and explained the various effective factors on it. This kind of response is simply obtainable by the structure of the AFA elements.

Here, we also explored the effects of the thickness and the permittivity of the substrate in the simple symmetric structure of the cell presented in Figure 2.6 (a) as well. We expect that since the effective permittivity that the circular slot in the middle layer sees is majorly a function of the dielectric permittivity and the dielectric thickness, the second resonance of the structure (in Figure 2.7) would be the most influenced parameter. The effective permittivity is proportional to the dielectric permittivity and dielectric thickness; therefore, by increasing the dielectric thickness or/and dielectric permittivity, the second resonance would shift to lower frequencies.

However, as discussed before, that is not the only effect that the dielectric slabs have in an AFA element. As a consequence of changing the electrical length of the slot in the middle layer, the amount of the coupling between the first and the third layers changes and that causes a secondary frequency to appear. Figure 3.6 shows how the frequency of this secondary resonance changes regarding the dielectric thickness of the slabs between the metallic layers. We can see when the

thickness is reduced from 1.27mm to 1mm, the coupling becomes strong enough so that the "doubled resonator" effect appears.

By reducing the dielectric thickness further, we can see while the resonance frequency at 10.5GHz (main resonance) is fairly fixed, the frequency of the secondary resonance changes. We can also see the effect of dielectric thickness in the second resonance in this figure as it was explained before. Therefore, the dielectric thickness can be altered to also change the ratio between the second and the first main resonances of the structure.

In Figure 3.7, we demonstrated the effect of the substrate relative permittivity on the three resonances of the structure and also on the secondary resonances. It is transparent that the higher permittivity lowers the resonance frequencies, but this parameter is more effective on the second and the third resonances since they are respectively related to the middle slot layer and the third ring layer. Furthermore, the substrate permittivity can be used to both change the ratio between the resonances of the structure and appearance of the secondary resonance of coupled elements.

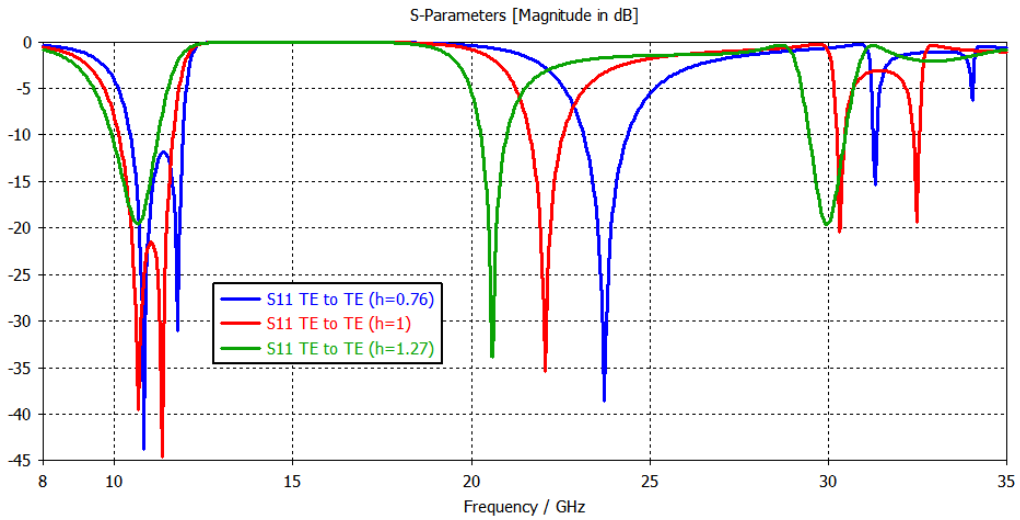

Figure 3.6 The effect of dielectric thickness in the frequency response of the AFA cell (the cell response to TE incident wave and TM incident wave is the same as the structure is symmetric regarding x and y axes).

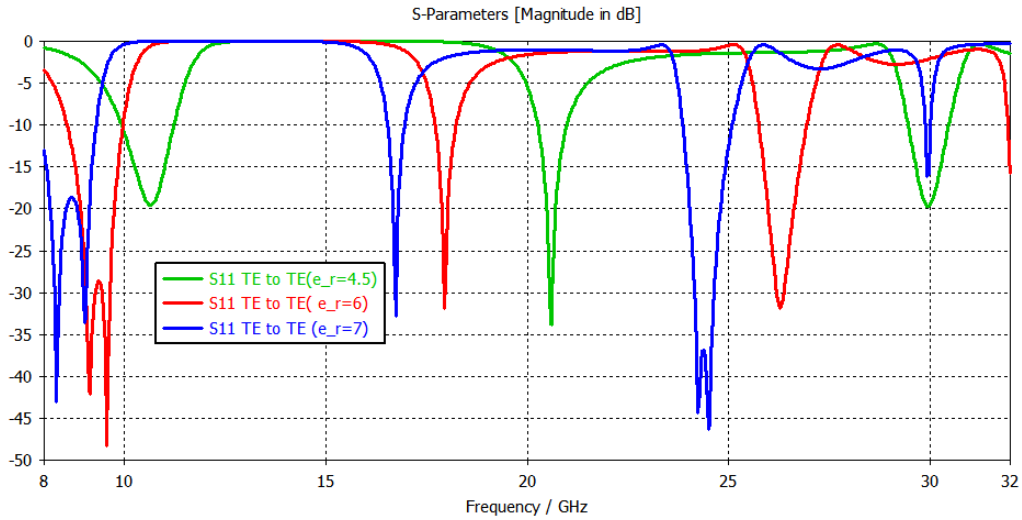

Figure 3.7 The effect of dielectric permittivity in the frequency response of the AFA cell.

Moreover, the transmission coefficients, depicted in **Error! Reference source not found.**5, rove that the structure meets the design requirements. The two LP transmission coefficients have equal values and 180˚-phase difference at 10.8 GHz and 16.7 GHz. The circular S-parameters are shown in Figure 3.8. It can be seen from Figure 3.8 that at both 10.8 GHz and 16.7 GHz, the cross-CP transmission coefficients are -0.8 dB and -0.4 dB, respectively. All the reflection coefficients and co-transmission coefficient are below -10 dB at both frequencies. These results were expected based on the equations presented in chapter 1. As a result, the sense of the incident wave changes as it goes through the unit-cell while the magnitude almost stays the same. Figure 3.88 also suggests that the AR of a CP wave illuminating the TA of this unit-cell at the upper frequency stays almost unchanged. However, the performance of the unit-cell in regard with AR can be improved by acceptance of some loss in the transmission coefficient at the lower band.

Table 3.1

Dual-Band Unit-Cell Dimentions

Parameter	**value (mm)**	**Parameter**	**value (mm)**
P_x	1.1	s	1.53
P_y	4.2	g_y	0.2
W	0.15	g_x	2.7
$R_1 = R_2$	2.94	h	0.76

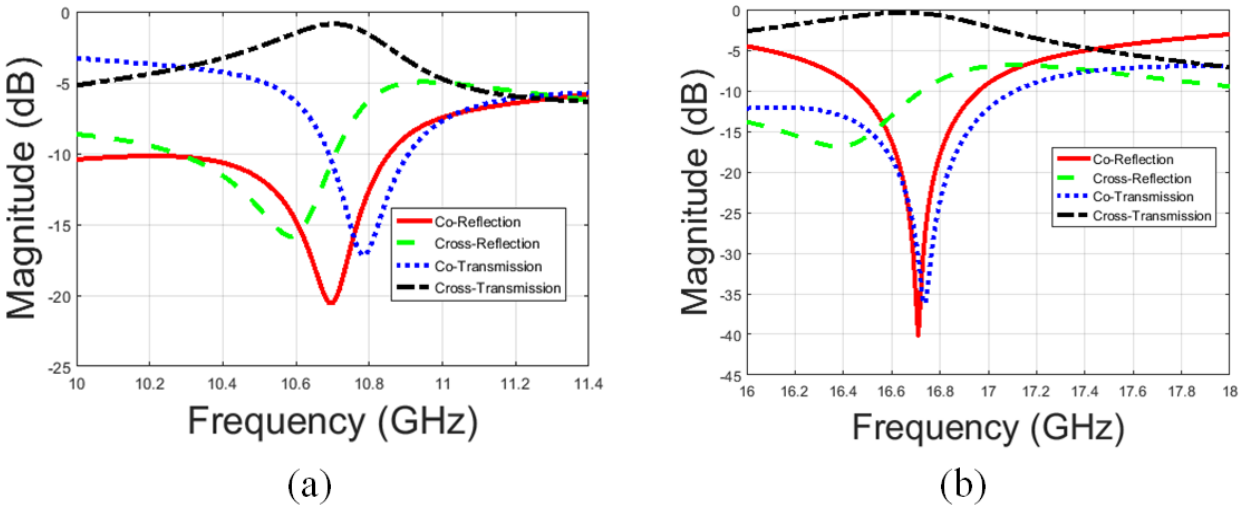

Figure 3.8 Circular scattering parameters of the proposed structure for the normal incident wave at (a) lower band and (b) higher band.

Next, the cell is rotated up to 180˚ with 10˚-steps in xy-plane at both 10.8 GHz and 16.7 GHz. We already expect a phase shift in transmission coefficient with the twice amount of the rotation angle by physically rotating the unit-cell. As a result, up to 360-degree phase shift is obtainable by rotating the unit-cell up to 180 degrees. The results presented in Figure 3.99 prove our expectation right at both frequencies.

Furthermore, since different elements on the TA surface can receive the illuminating wave with different incident angles, it is very important that the transmission coefficient stays fairly

constant and close to 0dB for different incident angles. Figure 3.1010 shows that there is no reduction of more than 1 dB in the transmission coefficient at both frequencies for incident angles up to 60° as compared to the normal incident.

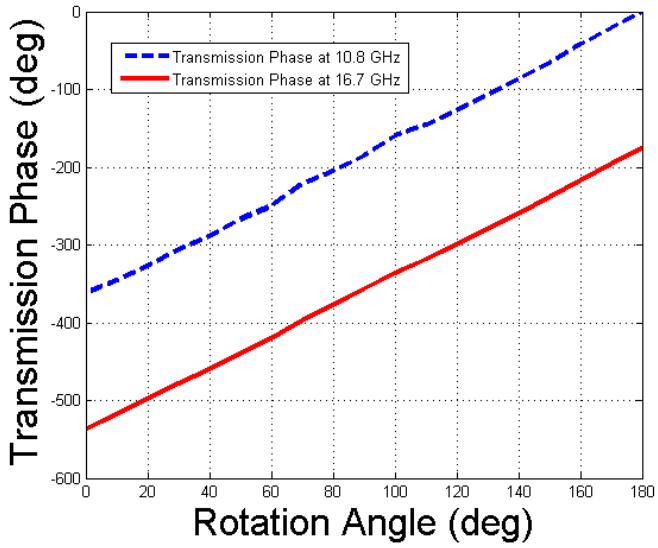

Figure 3.9 Variation of phase of the cross-transmission coefficient at 10.8 GHz and 16.7 GHz with rotation angle for normal incident wave.

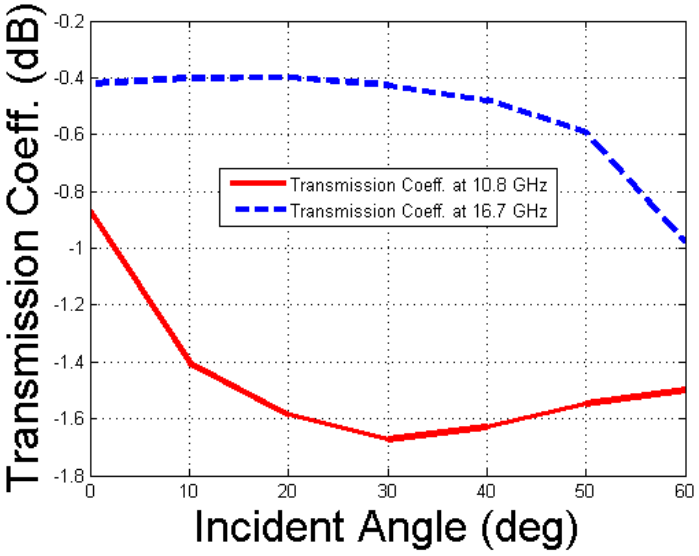

Figure 3.10 Variation of the magnitude of cross-transmission coefficient with incident angle at 10.8 GHz and 16.7 GHz.

All the simulation results presented in this section confirm that the proposed structure is a good candidate for dual-band circular-polarization TA applications. A prototype composing of two adjunct unit-cells was fabricated and tested. In order to measure the unit-cell's characteristics at both bands, the prototype was placed in WR62 and WR75 waveguides. As mentioned earlier, we ran all the previous simulations with periodic boundary conditions. However, to compare the measurement and simulation results at this step, we simulated the fabricated structure with all perfect electric conductor (PEC) boundary condition on all sides (See Figure 3.1111). The structure is then illuminated with TE_{01} mode electric field. The reflection and transmission coefficients of this prototype are plotted in Figure 3.122. Since the frequency range of WR75 is 10GHz to 15GHz, Figure 3.12 presents the behavior of the cell in this frequency range. It can be seen that the results of the similar simulated setup are in agreement with the measured results. Unfortunately, the measurement results in WR62 were not presentable due to fabrication errors and unavailability of suitable calibration kit.

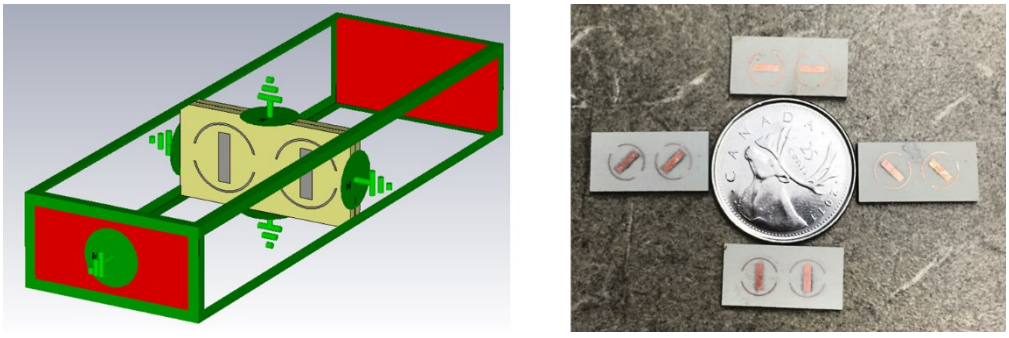

Figure 3.11 Two adjunct unit-cells with PEC boundary conditions on the sides simulating waveguide measurement setup (left) and fabricated unit-cells (right).

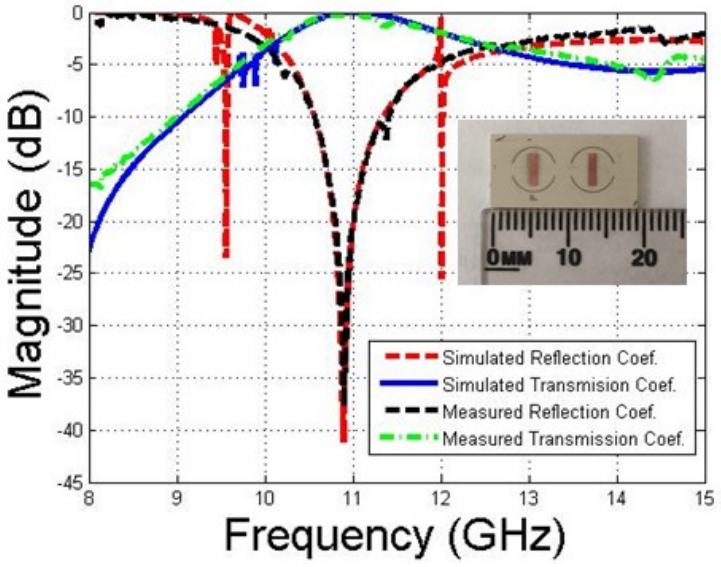

Figure 3.12 Simulation and measurement results of two unit-cells with zero rotation angle in a WR75 waveguide.

3.3 Conclusion

A novel dual-band circularly polarized TA unit-cell operating at 10.8 GHz and 16.7 GHz was presented in this paper. An array of the proposed unit-cell is able to concentrate the incident circularly polarized waves from a dual-band feed source to the pencil beam patterns in a desired direction by providing different transmission characteristics for the two orthogonal polarizations. To do so, the unit-cell is impedance matched for both polarizations while introducing a 180° difference between the transmission phases of the two orthogonal components of the incident wave at the frequencies of interest. The proposed unit-cell was fabricated and the lower band performance was tested in a WR75 waveguide. The measurement results and simulation results concur. The results demonstrate that the presented unit-cell can be employed as an element of a dual-band circular-polarized TA with minimum insertion and quantization loss.

Chapter 4

4 Conclusion and Future Work

In this chapter, we first summarize the contribution of this thesis and conclude our work. As the last section, we discuss the future research directions in this field.

4.1 Overall Contribution

This thesis proposed two separate, but related, novel unit-cells for TAs in satellite communication. Both proposed unit-cells are based on AFA structures while one operates in a single frequency-band and the other one is dual-frequency-band. AFA-based cells can be considered as spatial filters like FSS; once they are designed properly, they can manipulate the magnitude and phase of the normal incident waves. We utilized this capability to introduce phase shift to the transmitted wave through the cell itself. The goal is to achieve appropriate phase distribution with minimum insertion loss across a TA composed of minimum substrate layers and via-less elements.

4.1.1 Single-band CP Unit-Cell

As discussed in Chapter 2, a single-band unit-cell consisting of three metal layers was proposed. The metal layers included the receive antenna, non-radiating resonant coupling layer, and the transmit antenna. The receiving and transmitting antennas in each cell consisted of miniaturized

elements which are asymmetric regarding x- and y-axes. This asymmetry made the unit-cell behave differently to x- and y-directed electric fields in a way that the cell transmits both waves with equal magnitude and 180˚ phase difference. Therefore, the proposed cell can transmit a CP incident wave with the change of polarization sense to the other side. By changing the sense of CP polarization, the cell also functions as a phase shifter once it is rotated in xy-plane. Up to 360˚ continuous phase shift was achieved by the ERT. Compared to current solutions, this cell has the advantage of only 0.5dB insertion loss at 20.7GHz, providing continuous phase shift with minimum optimization required, including only two substrate layers, and operating in circular polarization.

4.1.1.1 Single-Band CP Transmit-Array System

As the first section of Chapter 2 explained, we configured the proposed unit-cell in two different TAs, each of which composed of 196 elements. The only variation between these TAs is their phase distribution to redirect the radiation from a low-gain feed antenna to high-gain pencil beam directed at broadside and 15˚-off broadside. We used 2×2-arrays of sequentially rotated CP patch antennas with 13dB gain and AR better than 1dB as the feed antennas. As the next step, we placed the TA in $F = 72.5\text{mm}$ which is $0.8 \times$ array side dimension from the feed antenna. It has been shown in the simulation and measurement results that the broadside TA system has 23.5dB gain at 20.5GHz with no more than 3dB decline in the band 19GHz-23GHz. The aperture efficiency of the system is 47% at 20.5GHz. Moreover, the AR in this band is better than 3dB. Afterwards, we replaced the broadside TA with 15˚ and 30˚ ones. The gains of these systems are 22.7dB and 21.5dB at the main beam direction, respectively. The AR of both systems remains

less than 3dB at 15˚ and 30˚ off broadside. Therefore, we proposed a wide-band single-band circular-polarized TA system with less than $9.1\text{cm width} \times 9.1\text{cm length} \times 77.5\text{cm heigh}$.

4.1.1.2 Same Sense Bidirectional CP Antenna

In the second section of Chapter 2, a slot antenna combined with FSS was designed to achieve same sense CP radiation at both sides of the antenna. This kind of antenna is required in applications where only one sense of CP radiation is desirable. We exploited the different behaviors of the proposed cell to the two perpendicular linear polarizations to change the sense of the CP polarization. The dimensions of the cell were scaled so that it operates at 1.7 GHz. Then, the proposed cell was structured in a uniform 3×3 FSS and it was placed in close distance of a bidirectional L-shaped slot antenna operating at the same frequency to convert the LHCP radiation to RHCP radiation at one side. Although comparing solutions with the similar insertion loss and number of substrate layers are available, this work is a proof of concept that this unit-cell can be utilized as a CP polarization convertor as well.

4.1.2 Dual-Band CP Unit-Cell

A novel dual-band circularly polarized TA unit-cell operating at 10.8 GHz and 16.7 GHz was presented in Chapter 3. This unit-cell is composed of three metallic layers that are easy to fabricate. The total thickness of the element is 2.54mm that is equal to $0.054\lambda_0$ (free-space wavelength) and $0.084\lambda_0$ at lower and upper frequencies, respectively. It is worth mentioning that the Rogers TMM4 laminate ($\varepsilon_r = 4.5$ and $tan\delta = 0.002$) was chosen as the substrate layers. This choice of substrate made the resonance length of miniaturized metallic elements fit in in the

cell with width and length of 7.6mm. This length corresponds to $0.27\lambda_0$ and $0.42\lambda_0$ at 10.8GHz and 16.7GHz, respectively. Therefore, since the size of the cell is smaller than $0.5\lambda_0 \times 0.5\lambda_0$, no extra side lobes appears in the transmitted power at either of the operational frequencies. As a result, an array of the proposed unit-cell is able to concentrate the incident circularly polarized waves from a dual-band feed source to the pencil beam patterns in a desired direction by providing different transmission characteristics for the two orthogonal polarizations. To do so, the unit-cell is impedance matched for both polarizations while introducing a 180° difference between the transmission phases of the two orthogonal components of the incident wave at the frequencies of interest. The proposed unit-cell was fabricated and the lower band performance was tested in a WR75 waveguide. The measurement results and simulation results concur. The results demonstrate that the presented unit-cell can be employed as an element of a dual-band circular-polarized TA with minimum loss.

4.2 Future Research

Although a great amount of research has been done on spatial filters such as FSS, AFA-based structures have not been explored to their full capacity. As demonstrated in this thesis, AFA elements can be composed of less substrate layers to achieve more number of supported frequency bands and wider bandwidth. Thus, this set of structures can open new horizons to address current shortcomings of wireless and point-to-point communications. In the following, we define a few further research suggestions.

4.2.1 Dual-Band Same Sense Bidirectional CP Antenna

The structure presented in the second section of Chapter 2 operates at one frequency band. It was proved in this thesis that the proposed unit-cell can be structured in FSS and function as a polarization convertor. However, the demand for dual-band and multiple-band operation in current wireless systems has been increased. For further research, the unit-cell proposed in Chapter 3 can be configured in a uniform array. The designed FSS, then, can be combined with a dual-band or wide-band bidirectional slot antenna to achieve same sense CP radiation at both sides of the radiating element at two frequency-bands.

4.2.2 Dual-Band CP Transmit-Array

Although the element presented in Chapter 3 operates at two frequency-bands, the phase shifts in the transmitted wave at these two frequencies are dependent and cannot be controlled independently. Therefore, to configure this cell in a TA, we need to quantize the required phase distribution on the TA's surface. However, further research can be done to alter the cell's structure in a way that the available phase shift at the two frequencies become independent. As a result, the insertion loss and quantization loss can be maintained minimum as well as the number of substrates.

Bibliography

[1] S. Ye, X. Liang, W. Wang, R. Jin, J. Geng, T. S. Bird, and Y. J. Guo, "High-gain planar antenna arrays for mobile satellite communications," IEEE Antennas and Propag. Mag., vol. 54, No. 6, pp. 256 - 268, Dec. 2012.

[2] R. V. Gatti, L. Marcaccioli, E. Sbarra, and R. Sorrentino, "Flat array antenna for Ku-band mobile satellite terminals," Proc. 5th European Conf. Antennas and Propag. (EuCAP), pp. 2618 - 2622, Rome, Italy, April 2011.

[3] Y. J. Cheng, P. Chen, W. Hong, T. Djerafi, and K. Wu, "Substrate-integrated-waveguide beamforming networks and multibeam antenna arrays for low-cost satellite and mobile systems," IEEE Antennas and Propag. Mag., vol. 53, No. 6, pp. 18 - 30, Dec. 2011.

[4] L. A. Greda and A. Dreher, "Tx-terminal phased array for satellite communication at Ka-band," Proc. 37th European Microwave Conf., pp. 266 - 269, Munich, Germany, Oct. 2007.

[5] J. Y. Lau, "Reconfigurable transmit-array antennas," Ph. D. dissertation, Dept. Elec. & Comp. Eng., Univ. Toronto, Ont., 2012.

[6] Technical Note 1: "State-of-the-art Review and Consolidated Requirements", KaLENS project, IT/AP/KaLENS/TN/01/v0, Feb 2014.

[7] M. C. Viganó, D. L. del Río, F. Bongard, J. Padilla, and S. Vaccaro, "One-bit phased array with wide scan and linear polarization control for mobile satellite applications," Proc. 6th European Conf. Antennas and Propag. (EuCAP), pp. 1641 - 1644, Prague, Czech Republic, March 2012.

[8] Kaplan, I., M. G. Gachev, B. Moshe, D. Spirtus, D. F. DiFonzo, K. A. Bruestle, R. Yip, V. Boyanov and Y. Gat (2010). Applications for low profile two way satellite antenna system, US Patent 7705793.

[9] G. Bellaveglia, L. Marcellini, R. Lo Forti, A. Arcidiacono, and B. Ray, "Low profile Ku-band VSAT antenna system for high-speed trains," 29th ESAAntenna Workshop on Multiple Beams and Reconfigurable Antennas, ESA/ESTEC Noordwijk, May 2007.

[10] R. Lo Forti, G. Bellaveglia, A. Colasante, E. Shabirow, and M. Greenspan, "Mobile communications: High-speed train Antennas from Ku to Ka," Proc. 5th European Conf. Antennas and Propag. (EuCAP), pp. 2354 - 2357, Rome, Italy, April 2011.

[11] H. Bayer, A. Krauss, R. Stephan, and M. A. Hein, "A dual-band multimode monopulse tracking antenna for land-mobile satellite communications in Ka-band," Proc. 6th European Conf. Antennas and Propag. (EuCAP), pp. 2357 - 2361, Prague, Czech Republic, March 2012.

[12] J. R. Costa, C. A. Fernandes, G. Godi, R. Sauleau, L. Le Coq, and H. Legay, "Compact Ka-band lens antennas for LEO satellites", IEEE Trans. Antennas and Propag., vol. 56, pp. 1251 - 1258, May 2008.

[13] J. Thornton, A. White, and G. Long, "Multi3333-beam scanning lens antenna for satellite communications to trains," Microwave Journal, Aug. 2009.

[14] T. Maruyama, K. Yamamori, and Y. Kuwahara, "Design of multibeam dielectric lens antennas by multiobjective optimization," IEEE Trans. Antennas and Propag., vol. 57, pp. 57 - 63, Jan. 2009.

[15] L. Moustafa, R. Gillard, F. Peris, R. Loison, H. Legay, and E. Girard, "The Phoenix cell: A new reflectarry cell with large bandwidth and rebirth capabilities", IEEE Antennas and Wireless Propagation Letters, vol. 10, pp. 71-74, 2011.

[16] H. Kaouach, L. Dussopt, J. Lantéri, Th. Koleck, and R. Sauleau, "Wideband low-loss linear and circular polarization transmit-arrays in V-band," IEEE Trans. Antennas Propag., vol. 59, no. 7, pp. 2513–2523, July, 2011.

[17] H. F. Ma, B. G. Cai, T. X. Zhang, Y. Yang, W. X. Jiang, and T. J. Cui, "Three- dimensional gradient-index materials and their applications in microwave lens antennas," IEEE Trans. Antennas and Propag., vol. 61, pp. 2561 - 2569, May 2003.

[18] Lo, Y. T. & Lee. S. W. "Antenna Handbook". Vol. II: Antenna Theory. Edited by Van Nostrand Reinhold. New York. U.S.A. 1993. pp. 16-50 – 16-52.

[19] R. W. Wood, Physical Optics, (New York: Macmillan, 1905), pp. 86-91.

[20] D. Kwon and D. H. Werner, "Transformation electromagnetics: an overview of the theory and applications," IEEE Antennas and Propag. Mag., vol. 52, No. 1,pp. 24 - 26, Feb. 2010.

[21] F. Khosravi, “Applications of frequency selective surfaces in polarization control of antennas,” M. S. Thesis, Dept. Elec. & Comp. Eng., Univ. Alberta, AB, 2014.

[22] Rudi H. Phillion and Michal Okoniewski, “Lenses for circular polarization using planar arrays of rotated passive elements,” IEEE Trans. Antennas Propag., vol. 59, no. 4, pp. 1217–1227, April, 2011.

[23] E. Erdil, K. Topalli, O. Zorlu, T. Toral, E. Yildrim, H. Kullah and O. A. Civi, “A reconfigurable microfluidic transmitarray unit cell,” European Conference on Antennas and Propagation (EuCAP), Sweden, April, 2013.

[24] Technical Note 2: “Preliminary Antenna Design and Technology Investigations”, KaLENS project, IT/AP/KaLENS/TN/02/v0, Jan 2015.

[25] Nader Behdad, “A second-order band-pass frequency selective surface using nonresonant subwavelength periodic structures,” *Microwave and Optical Technology Letters,* vol. 50, no. 6, pp. 1639-1643, June, 2008.

[26] H. Kaouach, L. Dussopt, R. Sauleau, and T. Koleck, “Design and demonstration of an X-band transmit-array,” presented at the 3rd European Conference on Antennas and Propagation EuCAP, Berlin, 2009.

[27] J. Y. Lau and S. V. Hum, “A wideband reconfigurable transmitarray element,” IEEE Trans. Antennas Propag., vol. 60, No. 30, pp. 1303- 1311, March 2012.

[28] R. Brown and R. Dodson, “Parasitic spiral arrays,” in IRE Int. Convention Record, Mar. 1960, vol. 8, pp. 51–66.

[29] D. Pozar, “Flat lens antenna concept using aperture coupled microstrip patches,” Electron. Lett., vol. 32, no. 23, pp. 2109–2111, 1996.

[30] K.-W. Lam, S.-W. Kwok, Y. Hwang, and T. K. Lo, “Implementation of transmitarray antenna concept by using aperture-coupled microstrip patches,” in Proc. Asia-Pacific Microwave APMC’97, 1997, vol. 1, pp. 433–436.

[31] E. B. Lima, S. A. Matos, J. R. Costa, C. A. Fernandes, and N. J. G. Fonseca, “Circular Polarization Wide-Angle Beam Steering at Ka-Band by In-Plane Translation of a Plate Lens Antenna,” IEEE Trans. Antennas Propag., vol. 63, no. 12, pp. 5443-5455, Oct., 2015.

[32] S. Datthanasombat, J. Prata, A. L. R. Arnaro, J. A. Harrell, S. Spitz, and J. Perret, “Layered lens antennas,” in Proc. IEEE Antennas and Propagation Society Int. Symp., 2001, vol. 2, pp. 777–780.

[33] C. G. M. Ryan, M. R. Chaharmir, J. Shaker, J. R. Bray, Y. M. M. Antar, and A. Ittipiboon, “A wideband transmitarray using dual-resonant double square rings,” IEEE Trans. Antennas Propag., vol. 58, no. 5, pp. 1486–1493, 2010.

[34] P. Padilla, A. Munoz-Acevedo, and M. Sierra-Castaner, “Passive microstrip transmitarray lens for ku band,” presented at the4th Eur. Conf. on Antennas and Propagation EuCAP, 2010.

[35] H. Kaouach, L. Dussopt, R. Sauleau, and T. Koleck, “X-band transmitarrays with linear and circular polarization,” presented at the 4th Eur. Conf. on Antennas and Propagation EuCAP, 2010.

[36] A. Abbaspour-Tamijani, K. Sarabandi, and G. M. Rebeiz, “Antenna–filter–antenna arrays as a class of bandpass frequency-selective surfaces,” IEEE Trans. Microw. Theory Techn., vol. 52, no. 8, pp. 1781–1789, Aug. 2004.

[37] B. A. Munk, Frequency selective surfaces: theory and design. John Wiley & Sons, 2005.

[38] M. Li, M. Al-Joumayly, and N. Behdad, “Broadband true-time-delay microwave lenses based on miniaturized element frequency selective surfaces,” IEEE Trans. Antennas Propag., vol. 61, no. 3, pp. 1166–1179, Mar. 2013.

[39] M. Li and N. Behdad, “Wideband true-time-delay microwave lenses based on metallo-dielectric and all-dielectric lowpass frequency selective surfaces,” IEEE Trans. Antennas Propag., vol. 61, no. 8, pp. 4109–4119, Aug. 2013.

[40] S. M. A. Momeni Hasan Abadi and N. Behdad, “Design of wideband, FSS-based multibeam antennas using the effective medium approach,” IEEE Trans. Antennas Propag., vol. 62, no. 11, pp. 5557–5564, Nov. 2014.

[41] S. M. A. Momeni Hasan Abadi and Nader Behdad, “Wideband linear-to-circular polarization converters based on miniaturized-element frequency selective surfaces,” IEEE Trans. Antennas Propag., vol. 64, no. 2, pp. 525–534, Feb. 2016.

[42] L. Boccia, I. Russo, G. Amendola, and G. D. Massa, “Multilayer antenna-filter-antenna for beam-steering transmit-array applications,” IEEE Trans. Microw. Theory Tech., vol.60, no.7, Jul., 2012.

[43] H. Kaouach and A. Kabashi, “Antenna-Filter-Antenna based frequency selective surfaces for quasi-optical applications in Q-band,” presented at the 9th Eur. Conf. on Antennas and Propagation EuCAP, Lisbon, May, 2015.

[44] Ch. Cheng, A. Abbaspour-Tamijani, and C. Birtcher, “Millimeter-Wave beam-steering using an array of reconfigurable antenna-filter-antenna elements,” presented at IEEE MTT-S International Microwave Symposium Digest, San Francisco, CA, 2006.

[45] H. Kaouach, L. Dussopt, R. Sauleau, and Th. Koleck, “Design and demonstration of 1-bit and 2-bits transmit-array at X-Band frequencies,” 39th European Microwave Conference, Rome, Italy, Sept. 2009.

[46] M. P. DeLisio and R. A. York, “Quasi-optical and spatial power combining,” IEEE Transactions on Microwave Theory and Techniques, Vol. 50, No. 3, March 2002.

[47] L. Shafai. S. K. Sharma, L. Shafai, M. Daneshmand, and P. Mousavi, “Phase shift bandwidth and scan range in microstrip arrays by element frequency tuning,” IEEE Trans. Antennas Propag., vol. 54, no. 5, pp. 1467-1473, May, 2006.

[48] David M. Pozar, Microwave Engineering, John Wiley & Sons, 2012.

[49] E. Erdil, K. Topalli, N. S. Esmaeilzad, Ö. Zorlu, H. Kulah, and O. A. Civi, “Reconfigurable nested ring-split ring transmitarray unit cell employing the element rotation method by microfluidics,” IEEE Trans. Antennas Propag., vol. 63, no. 3, pp. 525–534, March, 2015.

[50] M. Euler and V. F. Fusco, “Frequency selective surface using nested split ring slot elements as a lens with mechanically reconfigurable beam steering capability,” IEEE Trans. Antennas Propag., vol. 58, no. 10, pp. 3417-3421, Oct., 2010.

[51] B. Strassner, C. Han, and K. Chang, “Circularly polarized reflectarray with microstrip ring elements having variable rotation angles,” IEEE Trans. Antennas Propag., vol. 52, no. 4, pp. 1122-1125, Apr., 2004.

[52] Ch. Han, Ch. Rodenbeck, J. Huang, and K. Chang, "A C/Ka dual frequency dual layer circularly polarized reflectarray antenna with microstrip ring elements," IEEE Trans. Antennas Propag., vol. 52, no. 11, pp. 2871-2876, Nov., 2004.

[53] A. Abbaspour-Tamijani, K. Sarabandi, and G. M. Rebeiz, "A millimetre-wave bandpass filter lens array," Microw. Antennas Propag., vol. 1, no. 2, pp. 388–395, Apr. 2007.

[54] James E. Raynolds, Ben A. Munk, Jonathan B. Pryor, and Ronald J. Marhefka, "Ohmic loss in frequency-selective surfaces," Journal of Applied Physics, vol. 93, no.9, pp. 5346-5358, May, 2003.

[55] "Material parameters" CST Suite Studio 2013 Manual.

[56] A. Clemente, L. Dussopt, R. Sauleau, P. Potier, and Ph. Pouliguen, "Focal distance reduction of transmit-array antennas using multiple feeds," IEEE Trans. Antennas Letters, vol. 11, pp. 1311-1315, 2012.

[57] M. Bozzi, S. Germani, and L. Perregrini, "Performance comparison of different element shapes used in printed reflectarrays," IEEE Antennas and Wireless Propag. Letters, vol. 2, pp. 219-222, 2003.

[58] A. Yu, F. Yang,A. Z. Elsherbeni, J. Huang, and Y. Rahmat-Samii, "Aperture efficiency analysis of reflectarray antennas," *Microwave and Optical Technology Letters,* vol. 52, issue 2, pp. 364-372, 2010.

[59] T. A. Milligan, Modern Antenna Design, 2nd ed. Hoboken, NJ: Wiley, 2005.

[60] P. Mousavi, B. Miners, and O. Basir, "Wideband l-shaped circular polarized monopole slot antenna," Antennas and Wireless Propagation Letters, IEEE, vol. 9, pp. 822–825, 2010.

[61] Ch. Liang, L. Li, and H. Zhai, "Variational stability form for the capacitance of an arbitrarily shaped conducting plate," *Chinese Journal of Electronics,* vol. 13, issue 4, pp. 714-718, 2004.

[62] F. Yang, A. Yu, A. Z. Elsherbeni, and J. Huang, "Single-layer multi-band circularly polarized reflectarray antenna: concept, design, and measurement," Electronics Letters, pp. 8-11, 2008.

[63] R. Pous and D. M. Pozar, “A frequency-selective surface using aperture couples microstrip patches,” IEEE Trans. Antennas Propag., vol. 39, pp. 1763–1769, Dec. 1991.

Publications

Journal Papers:

- P. Naseri, F. Khosravi, and P. Mousavi, "Antenna-filter-antenna-based transmit-array for circular-polarization application," IEEE Antennas and Wireless Propagation Letters (AWPL), DOI: 10.1109/LAWP.2016.2638469, 2016.

Conference Papers:

- P. Naseri, R. Mirzavand, and P. Mousavi, "Dual-band circularly-polarized transmit-array unit-cell at X and K-Bands," 10th European Conference on antennas and Propagation (EuCAP), Davos, Switzerland, April, 2016.
- P. Naseri, H. Moghadas, and P. Mousavi, " Ka-band circularly-Polarized reconfigurable transmit-array unit-cell," IEEE International Symposium on Antenna and Propagation (APS), Vancouver, BC, Canada, July, 2015.